THE ASTROPHYSICAL JOURNAL, 340:479–502, 1989 May 1

ENVELOPE STRUCTURES AND OPTICAL/RADIO POSITIONS OF COOL STARS[1]

P. F. BOWERS[2]
Sachs/Freeman Associates, Inc.
K. J. JOHNSTON
E. O. Hulburt Center for Space Research, Naval Research Laboratory
AND
C. DE VEGT
Hamburger Sternwarte, Universität Hamburg
Received 1988 July 5; accepted 1988 September 20

ABSTRACT

We report the results of sensitive 18 cm VLA observations of OH masers associated with the Mira variables IK Tau, U Her, R Aql, RR Aql, and the supergiant S Per. Astrometric optical positions of these stars and U Ori also are presented for comparison of the optical and radio reference frames. The linear radii of the OH shells range from about 35 AU to 450 AU, making these the smallest shells for which high-quality interferometric data have been obtained. We find evidence for axisymmetric structures in virtually all of the shells. For the smallest shell (U Her), the low- and high-velocity emission is separated into opposite quadrants on the sky relative to the star, similar to the case of U Ori. For the larger shells (IK Tau, R Aql), emission closest to the stellar velocity tends to lie along an axis on the sky which passes through the star's position, often manifesting itself as a double structure centered about the star. At the most extreme OH velocities, the maps for IK Tau and R Aql are complex, showing large angular displacements from the stellar position. The shell structure of RR Aql is highly asymmetric relative to the star.

Models invoking radial acceleration, rotation, or random velocity fluctuations do not provide a sufficient explanation of the observed complexities. We propose a model in which material is flowing from the star in a radially expanding ellipsoidal configuration. The total gas and dust density distribution thus varies with latitude from the equatorial plane. This model provides a way to explain numerous complexities in the angular distributions and profile structures of circumstellar OH masers which cannot be easily explained by the standard expanding spherical shell model. We conclude that axisymmetric outflow is common for red giants and supergiants and that the large magnetic field strengths observed for these stars may influence both the geometry and initiation of mass loss.

Subject headings: astrometry — interferometry — masers — stars: circumstellar shells — stars: long-period variables

I. INTRODUCTION

The standard expanding shell model provides a simple explanation for the characteristic, doubly peaked shape of OH maser profiles observed toward long-period variable stars. In this model radiation pressure quickly accelerates the dust which in turn accelerates the gas to a terminal velocity V_e. The OH is uniformly distributed in a thin shell and produces a doubly peaked profile shape with V_e equal to one-half the velocity separation of the peak features (Kwok 1976; Elitzur, Goldreich, and Scoville 1976; Reid *et al.* 1977; Sun and Kwok 1987). Paths of maximum maser gain occur along the line of sight to the star, so the peak features at velocities $V = V_0 \pm V_e$ are positionally coincident with the star. At velocities between the peak features and the stellar radial velocity V_0, the angular radius $\theta(V)$ is related to the shell radius θ_s by

$$\theta = \theta_s[1 - (V - V_0)^2/V_e^2]^{1/2} . \qquad (1)$$

There are many data directly confirming the basic predictions of this model at large radii ($R > 1000$ AU) in the envelopes via (*a*) measurements of the phase lag between the OH light curves of low-velocity (near) and high-velocity (far) emission features (Herman and Habing 1985) and (*b*) interferometric measurements of the $\theta(V)$ dependence of this emission (Booth *et al.* 1981; Baud 1981; Bowers, Johnston, and Spencer 1983; Chapman *et al.* 1984; Diamond *et al.* 1985; Herman *et al.* 1985; Chapman and Cohen 1986; Welty, Fix, and Mutel 1987). The data are based primarily on observations of the radio-luminous OH/IR stars (AGB long-period variables) and the OH supergiants. These stars have the largest OH shells and the highest OH luminosities (see Figs. 2 and 3 of Bowers 1985). For suitably nearby candidates ($D \leq$ a few kpc) the emission can be mapped over a wide velocity range between the peak spectral features, and the structure (kinematics and morphology) of the maser regions can be examined. For well-resolved cases, these data frequently show clumpy, approximately circular rings of emission at or near the stellar velocity, indicative of a spherical OH distribution (Bowers, Johnston, and Spencer 1983; Herman *et al.* 1985; Welty, Fix, and Mutel 1987). Axisymmetric OH distributions have been suggested in some cases, but these are usually OH supergiants (VY CMa, Bowers, Johnston, and Spencer 1983; IRC +10420, Diamond, Norris, and Booth 1983; VX Sgr, Chapman and Cohen 1986) or red giants with other peculiar properties (OH 231.8+4.2, Morris, Bowers, and Turner 1982; OH 19.2−1.0, Chapman 1988).

---

[1] Based on observations obtained at DSAZ–Calar Alto Observatory.

[2] Work performed at NRL under contract number N00014-86-C-2225.

At small radii ($R \leq 100$ AU), evidence for the expanding shell model is much weaker. The angular distributions (and often the profile shapes) of SiO and H_2O masers can be exceedingly complex and can change with time (e.g., Lane 1982; Johnston, Spencer, and Bowers 1985). Interpretation of the data in the context of this model includes discussions of thick shells or multiple shells at different expansion velocities combined with a healthy dose of turbulence (e.g., Diamond *et al.* 1987; Lane *et al.* 1987).

At intermediate radii, OH observations of classical, optically identified Mira variables indicate *consistency* with the expanding shell model from statistical considerations of the phase-lag measurements (Herman and Habing 1985) and from approximate positional coincidence of the outer peak spectral features (Bowers, Johnston, and Spencer 1983). The quality of the data generally are inadequate to rule out other contributions to the velocity field (e.g., rotation) or to say much about the morphology of the maser region (but see Bowers and Johnston 1988). Despite the proximity of these stars ($D < 1$ kpc), their small OH shell sizes and luminosities require that high spatial and spectral sensitivities be used to map the maser emission over a significant velocity range in the profile.

To improve our understanding of the structure of the OH maser region at radii between about 50 and 500 AU, we have obtained interferometric observations with relatively high angular resolution (1″), velocity resolution (0.3 km s^{-1}), and spectral sensitivity (0.3 Jy) for five optically identified Mira variables (IK Tau, U Ori, U Her, R Aql, RR Aql) and for the OH supergiant S Per. Astrometric optical positions of all of these stars also have been obtained to provide further information about the offset between the optical and radio reference frames (e.g., Johnston *et al.* 1985*a*; de Vegt *et al.* 1987). The observations are discussed in § II, and the results are presented in § III where the data are compared to the predictions of the standard expanding shell model. Virtually all of these stars show evidence for axisymmetric structures in their envelopes, and the $\theta(V)$ relationships for IK Tau and R Aql are not easily explained by the standard model. In § IV we determine that acceleration, rotation, or velocity fluctuations are minor kinematic components, and we conclude that a model in which the material is distributed in a radially expanding ellipsoidal configuration provides the best agreement with the properties seen in the available molecular data. In § V we suggest that models of mass loss driven by Alfvén waves may be extremely relevant for understanding both the initiation and geometry of mass loss in red giants and supergiants.

II. OBSERVATIONS

a) Radio

The 18 cm data were obtained during 1985 January 19 and February 9, using the NRAO[3] Very Large Array in its spectral line mode. Thirteen antennas were selected in the A-configuration with baseline lengths which ranged from about 3 to 34 km. All of the sources were observed in the right circular mode of polarization. The bandwidth was divided into 128 frequency channels, and on-line Hanning smoothing was applied to the data. The bandwidth was 195 kHz, resulting in a channel-to-channel frequency separation and resolution of 1.53 kHz. For IK Tau, the velocity extent of the OH emission exceeds the velocity range of this bandwidth. Two sets of integrations were therefore made at each hour angle for this star—one set centered on the low-velocity emission complex ($V = 17$ km s^{-1}), and one set centered on the high-velocity complex ($V = 50$ km s^{-1}).

A summary of the stars observed, the epoch, the number of hour angles for which data were obtained, the total integration time, the rest frequency, and the velocity resolution is given in Table 1. At each hour angle the star was observed for ~15 minutes and a nearby continuum point source was observed for ~5 minutes to calibrate the amplitudes and phases. The flux-density scale was established from observations of 3C 286 (1328+307) whose adopted flux density was 13.83 Jy at 1612 MHz and 13.61 Jy at 1666 MHz. Maps of the calibrated data were made for each spectral channel, cleaned with the standard algorithm of Högbom (1974), and restored with a Gaussian beam with a full-width half-power dimension of ~1″. The rms noise fluctuations ranged from ~40 mJy per beam per channel for S Per to 60 mJy per beam per channel for U Ori.

b) Optical

Optical positions of the stars S Per, U Ori, U Her, and R Aql have been obtained directly from plates taken with the 23 cm astrograph at the Hamburg Observatory. The primary reference frame is based on the AGK 3RN catalog (Corbin 1979) which is still the most homogeneous representation of the FK 4 system on the northern hemisphere. Since the plate field is 6° × 6°, an average number of 36 reference stars is available for the determination of the plate constants. Four plates for

TABLE 1

DETAILS OF RADIO OBSERVATIONS

Star	Epoch[a]	Number of Hour Angles	Integration Time (hr)	Frequency (MHz)	Velocity Resolution (km s^{-1})
S Per	1	7	1.6	1667	0.274
IK Tau[b]	1	6	1.3	1612	0.284
U Ori	1	2	0.5	1612	0.284
	1	2	0.5	1665	0.275
U Her	2	4	0.9	1667	0.274
R Aql	2	5	1.1	1612	0.284
RR Aql	2	4	0.9	1612	0.284

[a] Epoch 1 = 1985.05; epoch 2 = 1985.11.

[b] Two scans per hour angle.

---

[3] The National Radio Astronomy Observatory is operated by Associated Universities, Inc., under contract to the National Science Foundation.

TABLE 2

OPTICAL POSITIONS[a]

Star	α(1950)	δ(1950)	Besselian Epoch	μ_α (s yr^{-1})	μ_δ (arcsec yr^{-1})
S Per	$02^h19^m15^s.080$	+58°21′33″.61	1985.98	0.0000	+0.045
IK Tau[b]	03 50 43.750	+11 15 31.58	1985.92	...	...
U Ori	05 52 50.898	+20 10 05.93	1987.11	0.0000	−0.015
U Her	16 23 34.697	+19 00 17.76	1985.31	+0.0015	−0.006
R Aql[c]	19 03 57.702	+08 09 08.03	1983.53	−0.0014	−0.089
RR Aql[c]	19 55 00.309	−02 01 17.75	1984.01	...	...

[a] 1950 positions are given for the epoch of observation.

[b] Also known as NML Tau.

[c] Values from de Vegt *et al.* 1987.

each star have been taken in different orientations to the sky, very close and symmetric to the meridian. Exposure times were 5–10 minutes in all cases. A small spectral bandpass in the visual region 5200–5800 Å is utilized by this instrument, provided by a Kodak 103a-G + Schott OG 515 plate-filter combination which minimizes any influences of atmospheric dispersion and possible residual color errors in the telescope optics. A 4 mag grating has been used to control possible magnitude errors. The positions for these stars are unweighted means from all plates and multiple grating images per plate.

For the faint ($m_v > 14$) stars IK Tau and RR Aql, astrograph plates have been used to provide a system of secondary reference stars in the magnitude range $m_v = 12$–14; the plates of the stars have been taken with different long-focus telescopes. About 50–70 secondary reference stars have been selected in a 1° × 1° field centered at the star position. This field size is sufficient to cover the plate field of the long-focus plates. Positions of the secondary stars are based on four plates, each with a resulting positional accuracy of ±0″.06.

For RR Aql the 60 cm, F:15 refractor of the Hamburg Observatory was used; for details see de Vegt *et al.* (1987). In the case of IK Tau two plates were taken with the 2.2 m, F:7.7 RC reflector of the Calar Alto Observatory, using a Kodak 098-04 + Schott OG 550 plate-filter combination, which results in an approximate spectral bandpass extending from 5500 to 7000 Å. This telescope provides a scale of 12″ mm^{-1} and a high-quality field of ~1° diameter which makes it a very favorable instrument for astrometric work on faint objects (de Vegt *et al.* 1987). Both plates have been taken under good seeing conditions (<2″). The images of IK Tau do not show any deviation from the symmetric appearance of a stellar point source. In particular, no extended halo structure could be found from image processing of plate scans obtained with the Hamburg PDS 1010 G microdensitometer.

The resulting star positions based on the plate reductions obtained from the secondary reference stars agree within 0″.03 in both coordinates. The quoted position is the unweighted mean. This result is valid only for the adopted spectral bandpass of 5500–7000 Å; additional plates in the blue spectral region are necessary for further confirmation. Proper motions are taken from AGK 3 or from new observations of old epoch plates and are used to refer the optical positions from their epochs of observation to the epochs of the radio positions.

III. RESULTS AND ANALYSIS

a) Optical and Radio Positions

The B1950 optical positions (based on the FK 4 reference frame) and estimated proper motions are given in Table 2. The radio positions derived from the OH masers for all cases except R Aql are given in Table 3 and are relative to the radio reference frame defined by Witzel and Johnston (1982), which is estimated to be accurate to 0″.01. Also listed in Table 3 are the differences between the optical and radio measurements for both the FK 4 and FK 5 systems. Corrections for systematic differences between the FK 4 and FK 5 systems have been obtained from the tables of Schwan (1988) as applied to the AGK 3RN reference catalog. The correction in each coordinate is ≤0″.1.

The accuracy with which the absolute and relative radio positions of objects can be determined with the VLA is discussed by Johnston *et al.* (1985*a*, *b*) and Johnston, Migenes, and Norris (1989). The absolute position is determined relative to a background extragalactic radio source of known positional accuracy. If the target object (or maser feature) is unresolved, the accuracy with which the centroid of the emission can be determined with a high signal-to-noise measurement is the syn-

TABLE 3

RADIO POSITIONS AND DIFFERENCES (OPTICAL − RADIO) AT THE EPOCH OF THE OH MEASUREMENTS

	RADIO POSITIONS			(FK 4)		(FK 5)	
STAR	α(1950)	δ(1950)	BESSELIAN EPOCH	Δα cos δ	Δδ	Δα cos δ	Δδ
S Per	$02^h19^m15^s.090$	+58°21′33″.40	1985.05	−0″.08	+0″.17	−0″.12	+0″.10
IK Tau	03 50 43.719	+11 15 31.35	1985.05	+0.46	+0.23	+0.46	+0.19
U Ori[a]	05 52 50.909	+20 10 05.85	1985.05	−0.15	+0.11	−0.22	+0.16
U Her	16 23 34.692	+19 00 17.73	1985.11	+0.07	+0.03	−0.04	+0.08
R Aql[b]	19 03 57.687	+08 09 07.87	1985.11	+0.19	+0.02	+0.16	−0.02
RR Aql	19 55 00.309	−02 01 17.48	1985.11	0.00	−0.27	+0.04	−0.30

[a] Radio position from Bowers and Johnston 1988.

[b] Radio position from H_2O masers; see § III*e*(iv).

thesized beamwidth divided by the signal-to-noise ratio. If the background source is located within ~15° of the object, the relative position of the two sources can be found to 0″.1 with the VLA. With repeated hour angle coverage, this result can be refined to 0″.01 at frequencies higher than 5 GHz where the major source of error is differential phase path fluctuations between the antennas due to variations in atmospheric water vapor over the individual antennas. At lower frequencies (e.g., 1600 MHz) differential phase path variations caused by the ionosphere are important and are estimated to affect the positional accuracy at the 0″.05 level. For relative measurements over fields of a few arcseconds, accuracies of 0″.01 or better can be achieved.

To determine the radio positions, we have considered the positions indicated by (1) the outermost peak spectral features, (2) the extreme low- and high-velocity emission, and (3) least-squares fits of equation (1) to the data. For S Per, U Ori, U Her, and RR Aql, these positions agree to within 0″.05. All four of these stars have small shell radii ($\theta_s \leq 0''.5$), and the emission distributions are unresolved and positionally coincident (to within the errors) at the low- and high-velocity edges of the profiles. For RR Aql the OH position agrees to within 0″.02 with the mean position of the H_2O masers, providing an independent check of the accuracy of the OH position.

For IK Tau and R Aql the emission distributions are resolved and complex at the edges of the profiles, and we demonstrate in § III*e* that position determinations based on individual (or pairs of) spectral features are unreliable in such cases. Additional errors may be introduced by possible changes in the emission structure as a function of time (e.g., R Aql). The position given in Table 3 for IK Tau is derived from a least-squares fit of equation (1); the internal error from the fitting procedure is estimated to be about ±0″.05. The position of R Aql is based on the H_2O masers and has an estimated error of ±0″.15. There are indications from the OH data that this is the probable radio position of the star, but the complex shell structure prevents us from obtaining a reliable OH position by the standard methods.

Discrepancies of order 0″.2 between optical (FK 4) and radio continuum positions are typical for stars where both types of positions have been estimated to high accuracy (Johnston *et al.* 1985*a*). Attempts to determine stellar positions from OH masers lead to discrepancies of order 0″.3 (de Vegt *et al.* 1987). Table 3 shows that the discrepancies for all the stars except IK Tau are consistent with this latter level of accuracy. The angular size of the OH shell for IK Tau is large (2″ × 4″) and the envelope structure is complex, so it is possible that the larger discrepancy for this star is due not to systematic differences between the optical and radio reference frames but rather to the difficulty in determining the radio position from a simple outflow model for the shell structure.

b) Radial Velocities (V_0) *and Expansion Velocities* (V_e)

The values of V_0 and V_e derived from least-squares fits of equation (1) are listed in columns (2) and (3) of Table 4 for all the stars except U Ori and R Aql. This method is not used for these two stars because of complexities in their OH distributions. We list in parentheses the respective differences ($V_0^W - V_0$) and ($V_e^W - V_e$), where V_0^W and V_e^W are the mean and half-width of the velocity range in the OH profile. Values of V_0 and V_0^W agree to within 0.3 km s^{-1} (i.e., our velocity resolution), and values of V_e and V_e^W agree to within 1 km s^{-1}. The agreement of these two sets of values confirms that V_e is better represented by the half-width of the entire velocity range than by the half-width of the velocity separation of the outer peak features (also see Bowers, Johnston, and Spencer 1983). Large errors in determination of V_0 and V_e can occur if the velocity range of the emission is asymmetrically distributed relative to the true stellar velocity, as in the case of U Ori (Bowers and Johnston 1988). If the OH distribution strongly deviates from sphericity, V_e represents only the maximum outflow velocity along the line of sight (§ IV*b*).

c) Shell Radii, Thickness, and Mass-Loss Rates

The values of $\langle\theta_s\rangle$ in column (4) of Table 4 represent our best estimates of the average θ at $V = V_0$ based on measurements of the angular distance of discrete map components from the inferred radio position of the star. The errors are the rms uncertainties of the fits of equation (1), where applicable. The angular radii for R Aql and RR Aql are about a factor of 2 smaller than was estimated by Bowers, Johnston, and Spencer (1983); the differences reflect the higher quality of the present data.

The values of the ratio of the outer to inner shell radii (R_0/R_i) are listed in column (5) and have been estimated from the largest scatter of $\theta(V)$ at a given V. These values may be upper limits if the shell structure is complex (e.g., R Aql). The ratios are generally smaller than those of 2.5 to 4 estimated for three OH/IR stars by Bowers, Johnston, and Spencer (1983).

In columns (6), (7), and (8) we respectively list the distance D, the mean linear radius $\langle R\rangle$, and the mass-loss rate $\dot{M}$. In order of decreasing priority, $\dot{M}$ has been estimated from CO observations (Knapp and Morris 1985; Wannier and Sahai 1986), from the dust shell models of Rowan-Robinson and Harris (1983)

TABLE 4

SHELL PARAMETERS

Star (1)	V_0 (km s^{-1}) (2)	V_e (km s^{-1}) (3)	$\langle\theta_s\rangle$ (4)	R_0/R_i (5)	D (pc) (6)	$\langle R\rangle$ (AU) (7)	$\dot{M}/10^{-7}$ ($M_\odot$ yr^{-1}) (8)	Notes (9)	References for $\dot{M}$ (10)
S Per	−37.5(−0.1)	17.4(−0.7)	0″.05 ± 0″.05	...	2300	115	44.	1	1
IK Tau	33.2(+0.3)	18.7(−0.8)	1.65 ± 0.14	1.8	270	445	51.	2	2
U Ori	−39 ± 1	8 ± 1	0.21	1.6	250	54	0.8	3	3
U Her	−14.2(+0.2)	6.6(+0.4)	0.13 ± 0.04	2	270	35	1.2		1
R Aql	47.4	7.7	≈1.50	≈5	200	300	5.6	4	4
RR Aql	27.8(−0.1)	6.8(+0.5)	0.45 ± 0.05	2	320	144	1.3	5	1

NOTES.—(1) D from Humphreys 1975. (2) Possible second shell with $\theta_s = 3''.0$, but see model in § IV*b*. (3) Bowers and Johnston 1988. (4) V_0 and V_e are mean value and half-width of OH velocity range. (5) θ_s(near) = 0″.30; θ_s(far) = 0″.59.

REFERENCES.—(1) Rowan-Robinson and Harris 1983 and this paper; (2) Knapp and Morris 1985; (3) Netzer and Knapp 1987 and this paper; (4) Wannier and Sahai 1986.

along with the equations of Knapp (1985), or from the relation between the radius of the OH shell and the mass-loss rate (Netzer and Knapp 1987). The appropriate reference for $\dot{M}$ (and usually D) is given in column (10).

d) *Morphological and Kinematical Properties*

The stars discussed in this paper were chosen for the most part not for their exotic characteristics but as a representative sample of nearby Mira variables (and one supergiant) with relatively low mass-loss rates and small maser shells. Yet in every case except perhaps RR Aql we find evidence for a possible axisymmetric distribution of the OH emission. The evidence is provided in three ways. (1) For the smaller shells (U Ori, U Her), there is an angular separation of the low- and high-velocity features into opposite quadrants on the sky relative to the star. (2) For the larger shells (IK Tau, R Aql), the emission occurs at all position angles relative to the star when integrated over velocity but preferentially is located in opposite quadrants at many intermediate velocities, often manifesting itself as a double structure centered on the star. (3) In most cases the overall shape of the velocity-integrated emission distribution is elongated with an orientation of the major axis which is identical to that indicated by points 1 or 2.

We summarize in Table 5 the overall sizes and the orientations of the axes of symmetry based on one or more of the three points of evidence listed above. To examine further the possibility of axisymmetric structure, we also include information about the distributions of the H_2O masers, which usually also show elongated distributions. The data are taken from Diamond *et al.* (1987) for S Per, Lada *et al.* (1981) for U Ori, and Lane *et al.* (1987) for the remaining stars.

Interpretation of H_2O data is difficult because the shapes of the distributions can change with time, and it is difficult to locate the star relative to the maser features (Johnston, Spencer, and Bowers 1985). Nonetheless, Table 5 shows the extremely interesting result that the orientation of the H_2O masers tends to be orthogonal to that of the OH for S Per, U Ori, and R Aql. For IK Tau which has the largest OH shell (Table 4), the orientations are parallel over comparable velocity ranges (see note 2 to Table 5). A similar result has been found by Chapman and Cohen (1986), who indicate that the distribution of H_2O masers is orthogonal to the main-line OH masers in the inner envelope of VX Sgr and parallel to the 1612 MHz masers in the outer envelope. These results suggest that the relative orientations of the OH and H_2O masers are not random and that axisymmetric structures are present in the envelopes.

We also indicate in Table 5 consistency or inconsistency of the data with the $\theta(V)$ relationship predicted by the standard expanding shell model (eq. [1]). As noted previously, IK Tau and R Aql show extended, complex structures at the most extreme low and high velocities, indicating either complex spatial distributions or nonradial motions. This issue is addressed more fully in § IV.

e) *The Individual Stars*

In this section we present the OH profile for each star, maps of the angular distribution of OH as a function of the radial velocity, and plots of the angular radius θ of the emission region as a function of the velocity, where θ is the distance of discrete components from the inferred radio position of the star. Maps are presented at each velocity at which the emission is resolved, and the data are compared to the predictions of the standard expanding shell model (eq. [1]). Data and analysis for the complex case of U Ori are presented elsewhere (Bowers and Johnston 1988).

i) *S Per*

The 1667 MHz profile has changed significantly with time. Observations taken in the early 1970s (Baudry, LeSqueren, and Lépine 1977; Fillit, Proust, and Lépine 1977) show emission concentrated in two velocity ranges (-52 and -26 km s^{-1}), similar to the double-peaked profile structure at 1612 MHz (Bowers 1975; Dickinson, Kollberg, and Yngvesson 1975). The profile in Figure 1 shows that the emission is distributed over a wide velocity range (comparable to that at 1612 MHz), but the strongest emission is now at -45 km s^{-1}. The profile is similar to the profile of right circularly polarized emission published by Diamond *et al.* (1987) for epoch 1982 October, except that their profile shows emission between -41 and -38 km s^{-1} while ours does not. In comparison, the flux density at 1612 MHz varies with time, but the profile structure of that emission has not changed significantly (see Diamond *et al.*).

The OH main-line (1665/1667 MHz) masers recently have been mapped by Diamond *et al.* (1987) between velocities of -55 and -32 km s^{-1} with a spatial resolution of 0″3. They find this emission to be distributed over a region of 0″08 × 0″03, elongated in the north-south direction. Their mean

TABLE 5

MORPHOLOGICAL AND KINEMATICAL PROPERTIES

STAR	FREQUENCY (MHz)	OH		H_2O		NOTES	
		Overall Size	Orientation	Overall Size	Orientation	Morphology	Kinematics
S Per	1667	0″15 × 0.10	N–S	0″12	E–W	1	7
IK Tau	1612	3.5 × 2.3	NW–SE	0.33	NW–SE	1, 2	8
U Ori	1612	0.20	NE	0.3	NW–SE	1, 3	7
	1665	0.45	NE–SW			4	7
U Her	1667	0.35 × 0.20	E–W	0.15	?	1, 5	7
R Aql	1612	3 × 2	NE–SW	0.33	NW–SE	1, 6	8
RR Aql	1612	1	SW	0.16	?	3	7

NOTES.—(1) Velocity-integrated shape of OH distribution is elongated. (2) OH is preferentially NW or SE of star at most intermediate velocities, but NE and SW at the most extreme velocities (16 and 51 km s^{-1}). H_2O is NW–SE between 18.5 and 25 km s^{-1} and between 43 and 49.2 km s^{-1}, and is ringlike at intermediate velocities. (3) Most OH is asymmetrically located relative to the star. (4) Velocity-integrated shape is circular, but there is a NE–SW angular separation of low- and high-velocity emission. (5) E–W angular separation of low- and high-velocity emission. (6) OH is NE–SW at V closest to V_0. (7) Consistent with eq. (1). (8) OH at extreme velocities is complex and displaced from the inferred stellar position.

radius for the emission region is 0″.05, based on the assumption that the extreme low-velocity emission at -55 km s^{-1} indicates the stellar position.

Because of our better spectral sensitivity, we have been able to map all emission features in Figure 1 with a total flux density larger than 0.2 Jy, encompassing the velocity range from -55 to -22 km s^{-1}. A map of the absolute positions of the maser features is shown in Figure 2. All of the features observed with the VLA (*filled circles*) were unresolved. The positional coincidence of the extreme low (-55.2 km s^{-1}) and high (-21.6 km s^{-1}) velocity features at the origin of the map demonstrates that, to first order, an expanding shell model is appropriate in the region of the main-line OH masers and that the star is located at the origin of the map. The results of a least-squares fit of equation (1) to our data (Table 4) agree well with those determined by Diamond *et al.* (1987), but we consider our values to be of more limited significance because virtually all the VLA features are located at the origin of the map.

We include the MERLIN data of Diamond *et al.* as empty circles in Figure 2, where alignment of the two data sets is based on superposition of the low-velocity emission near -55 km s^{-1}. The VLA and MERLIN data are consistent with a possible north-south elongation for the majority of the emission features, but the ratio of the positional errors (VLA, ±0″.05; MERLIN, ±0″.03) to the shell radius is too large to allow definitive conclusions about the morphology.

ii) *IK Tau*

The emission profile at 1612 MHz is displayed in Figure 3 and shows emission ranging from 15.9 to 51.1 km s^{-1}. Four major peak features are present at velocities of 16.2, 17.3, 46.9, and 50.6 km s^{-1} and are labeled P1–P4, respectively. Profiles with comparable or better velocity resolution have been obtained at epoch 1976.9 by Silverglate *et al.* (1979) and at epoch 1977.9 by Fix (1987). Our profile differs from these earlier profiles in two respects. First, the flux densities of the peak features (P2–P4) in Figure 3 are larger than those in the profiles of Silverglate *et al.* and Fix by ratios of ~2.5 and 5.0, respectively. Second, the peak feature P1 is not clearly evident in the previous profiles, although there is a very weak (0.3 Jy) feature at the corresponding velocity in the profile of Fix (1987). Thus at 16.2 km s^{-1} the flux ratio (epoch 1985.05/1977.9) is ~10, much larger than the ratio of ~3 indicated by the peak-to-peak amplitude of the OH light curve (Herman and Habing 1985).

Maps are shown in Figure 4*a* for all low-velocity features and Figure 4*b* for all high-velocity features with a peak flux density larger than 0.2 Jy per beam. The emission is resolved at most velocities, although in such cases it generally appears to consist of pairs of unresolved components. The extreme high-velocity feature at $+51.1$ km s^{-1} is clearly extended, and there is some indication for complex structure in the extreme low-velocity feature at $+15.9$ km s^{-1}. The outermost low-velocity peak feature (P1) is located at the same position as the map maximum at 15.9 km s^{-1}. The outermost high-velocity feature (P4) consists of two components separated by 1″.17.

A map summarizing the absolute positions of the map components is displayed in Figure 5. At velocities where there are definite multiple peaks in the maps, the positions of all corresponding clean components are plotted. Low-velocity features ($V < 25$ km s^{-1}) are denoted by filled circles; high-velocity features ($V > 45$ km s^{-1}) are denoted by empty circles. The low- and high-velocity features generally are clustered in similar regions of the map.

Because the emission features at the outer edges (and peaks) of the OH profile are resolved, it is difficult to determine a highly accurate position for IK Tau. Our inferred position for the star has been determined by least-squares fits of equation (1) to the data for various assumed positions of the star, and the crosses in Figures 4 and 5 are located at the position of the best fit. With the exception of the three northern components at $V \approx 19$ km s^{-1}, the emission is located in a ringlike structure centered about this position (Fig. 5). However, Figure 4 shows that there is a tendency for emission at most velocities to originate southeast or northwest of the star. This result is par-

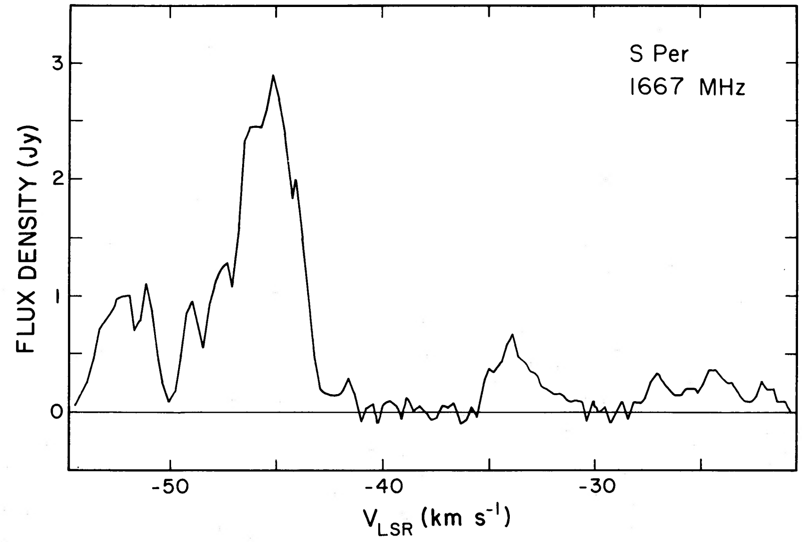

FIG. 1.—Spectral-line profile of the 1667 MHz emission from S Per

1989ApJ...340..479B

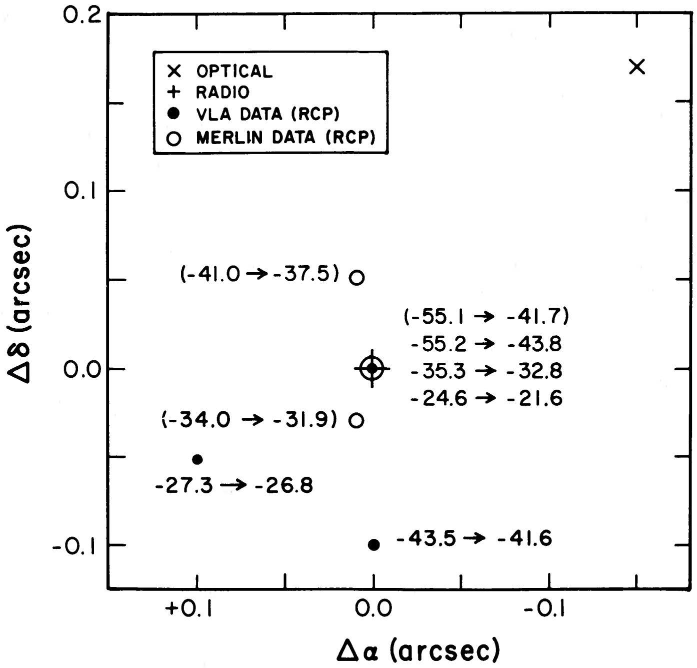

FIG. 2.—Absolute positions of the 1667 MHz emission components of S Per relative to the adopted radio position (*cross*). The "x" indicates the optical position corrected for proper motion to the epoch of the radio data. VLA data (epoch 1985.05; positional error ≈ ±0″.05) are plotted as filled circles, and the radial velocities are indicated nonparenthetically. MERLIN data (epoch ≈1983.0; positional error ≈ ±0″.03) are plotted as empty circles, and the radial velocities are indicated parenthetically.

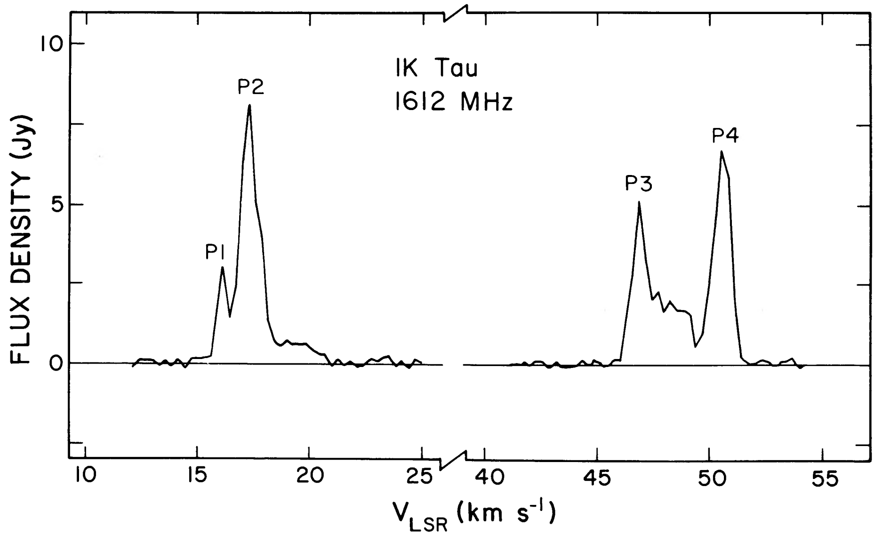

FIG. 3.—Spectral-line profile of the 1612 MHz emission from IK Tau

ticularly evident in Figure 4*b* where the emission over virtually the entire high-velocity range is confined to these two quadrants.

The angular distances of individual components from our adopted stellar position are plotted in Figure 6 as a function of the radial velocity. The broken curve shows the results of the best least-squares fit (Table 4) and indicates that the data are fitted reasonably well by a thin, expanding shell model at most velocities, but the three points between 18.7 and 19.2 km s^{-1} and the complex structures at the extreme velocities are not consistent with this model.

iii) *U Her*

The profile at 1667 MHz is displayed in Figure 7 and shows major peak features (P1–P4) with midpoint velocities of approximately -19.4, -16.6, -10.9, and -9.2 km s^{-1}. The shape of the profile is similar to those obtained by Fix (1987) and Sivagnanam *et al.* (1988), but the blueshifted peak features in their profiles are, respectively, 2.5 and 4 times stronger. All features with a flux density larger than 0.2 Jy were mapped and found to be unresolved. A map of the absolute positions of the features is shown in Figure 8. Filled and empty circles respectively indicate low- and high-velocity emission relative to the

1989ApJ...340..479B

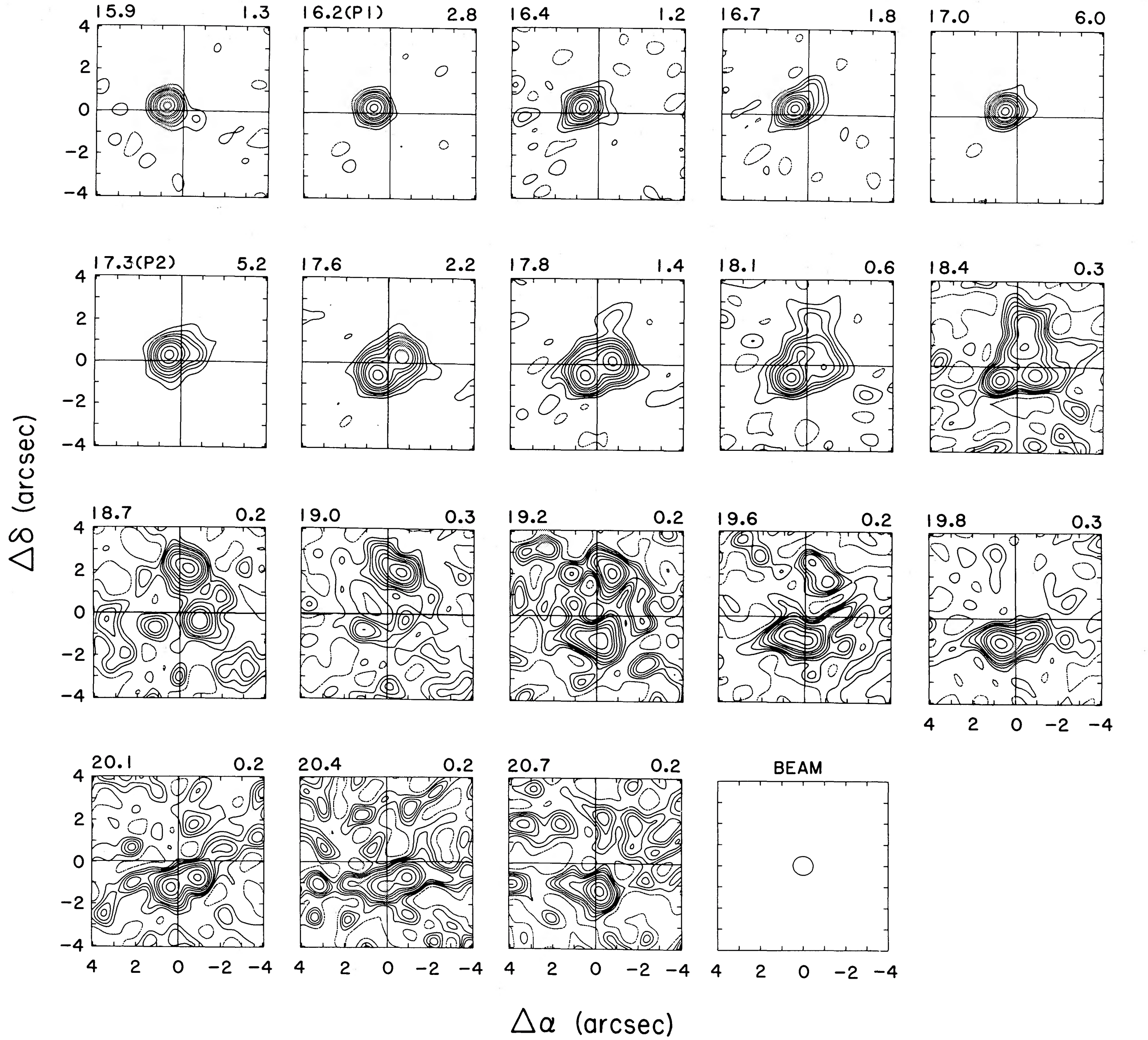

FIG. 4*a*

FIG. 4.—(*a*) Maps of the angular distribution of low-velocity ($V < V_0$), 1612 MHz emission for IK Tau at epoch 1985.05. The origin of each map is located at the adopted radio position. The LSR radial velocity (km s^{-1}) and peak flux density (Jy per beam) are indicated on each map. Contour levels are −5%, 5%, 10%, 15%, 20%, 30%, 40%, 50%, 70%, and 90% of the peak flux density. The fullwidth half-power synthesized beam is shown as the last map in the series. (*b*) Same as (*a*) for the high-velocity ($V > V_0$) emission.

stellar velocity ($V_0 \approx -14$ km s^{-1}).

Figure 8 shows that the emission distribution is elongated with an angular diameter of ~0".35 in the east-west direction and 0".20 in the north-south direction. There also is a velocity discontinuity (indicated by the diagonal line) in that the low-velocity emission is systematically eastward and southward and the high-velocity emission is westward and northward of the map origin. It is evident, however, that radial expansion is the dominant kinematic mode because features at velocities near the edges of the profile are located near the center of the emission distribution, while features near the stellar velocity are located at the far eastern and western edges of the distribution.

We have examined three criteria for determining the stellar position: (1) the mean position ($\Delta\alpha = +0''.008$, $\Delta\delta = +0''.018$) of the extreme low (−20.8 km s^{-1}) and high (−8.2 km s^{-1}) velocity features; (2) the mean position ($\Delta\alpha = +0''.008$, $\Delta\delta = -0''.008$) of the outer peak features (−19.9 and −9.2 km s^{-1}); and (3) the position ($\Delta\alpha = 0''.0$, $\Delta\delta = 0''.0$) derived from fitting equation (1) to the data for various assumed positions of the

1989ApJ...340..479B

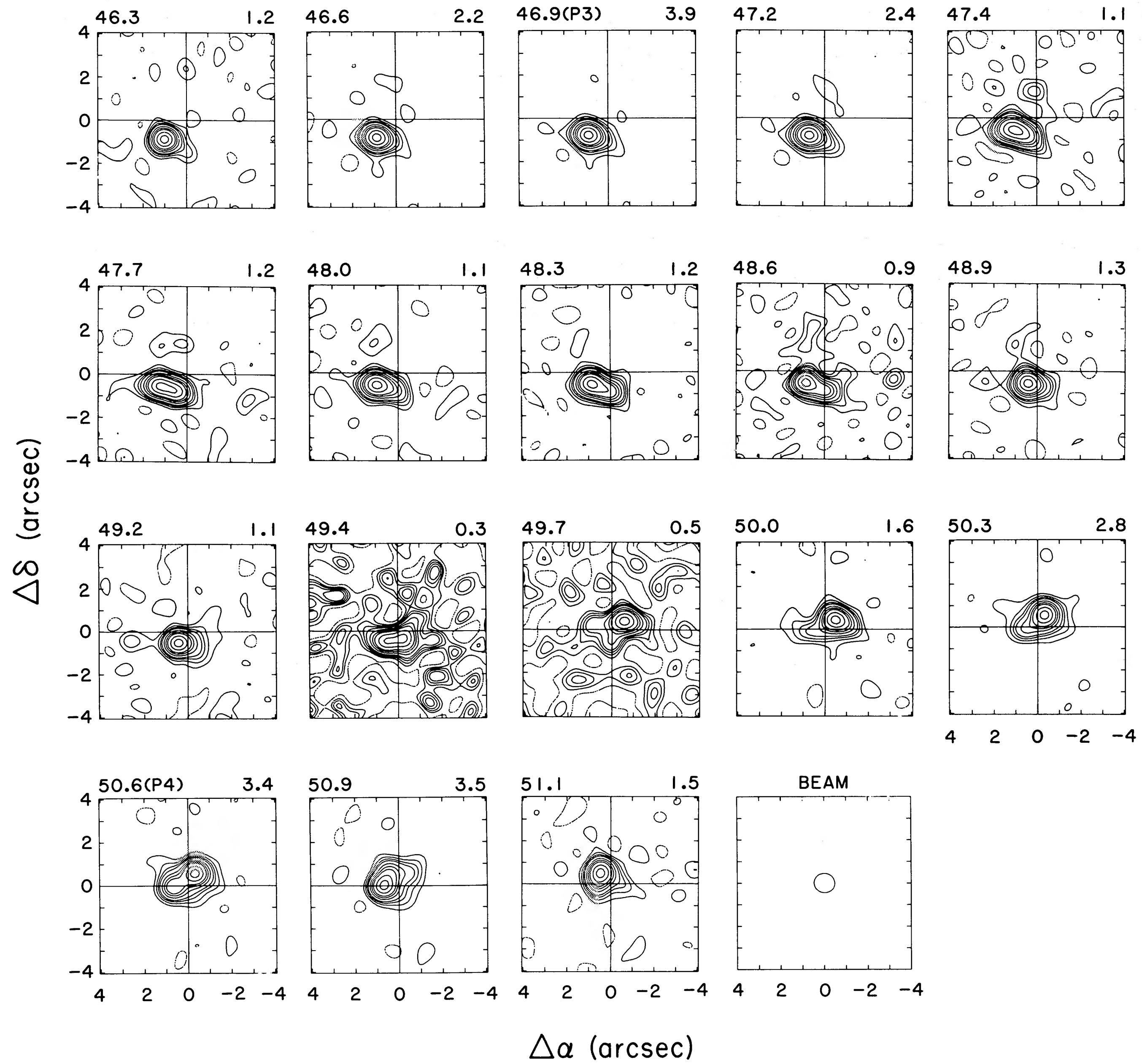

FIG. 4b

star. We adopt the latter position as the radio position of the star because the positional error of ±0ʺ.05 for individual components is large compared to the shell radius. The location of the −20.8 km s^{-1} feature in Figure 8 agrees with our inferred position to within the errors, supporting the suggestion by Sivagnanam *et al.* (1988) that the compact (≈23 milliarcsec) component at this velocity may be amplifying the stellar continuum. The resulting angular radius-velocity plot at our adopted position is shown in Figure 9, where the solid line is the least-squares fit of equation (1) (Table 4).

iv) *R Aql*

The 1612 MHz profile shape for this star is distinctive because of the abnormally large ratio (1:15) for the peak intensities of the low- and high-velocity groups. Figure 10 shows peak features at about 41.2, 43.5, and 54.0 km s^{-1} (P1–P3). Comparison to profiles obtained at other epochs (e.g., Fix 1987; de Vegt *et al.* 1987) indicates small changes in the shape of the low-velocity group of features as a function of time.

We have mapped all features in Figure 10 with a peak flux density >0.3 Jy per beam, corresponding to velocity ranges of 40.1–44.0 km s^{-1} and 52.6–54.8 km s^{-1}. Maps at all velocities with detectable emission are displayed in Figure 11 with the origin of the maps identical to that of VLA maps published by de Vegt *et al.* (1987) for this star. The emission is resolved at all velocities and its structure changes rapidly with velocity near the outer edges of the profile.

Comparison to the maps of de Vegt *et al.* shows that there

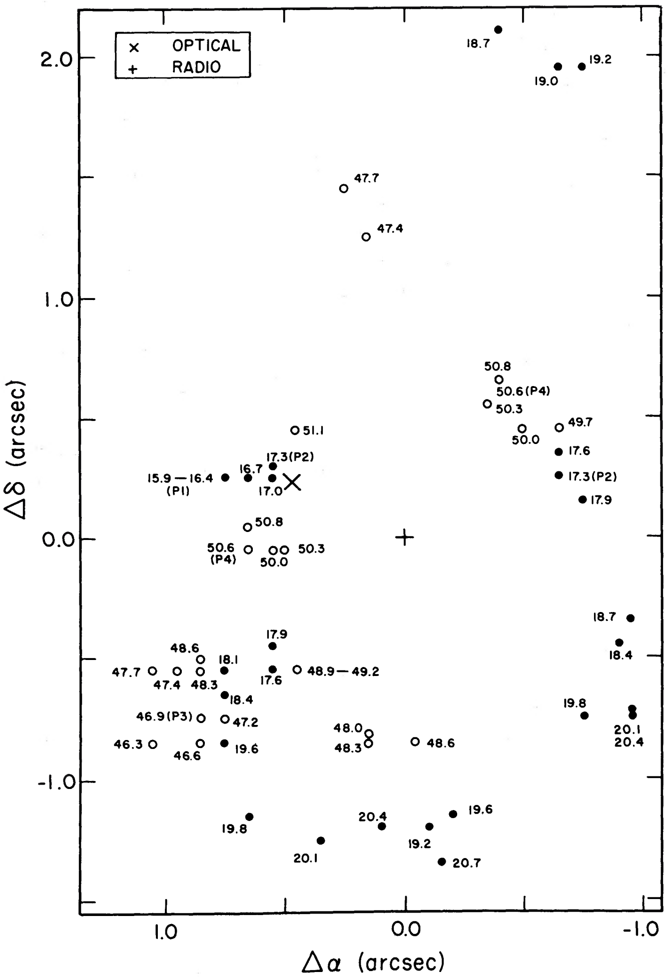

FIG. 5.—Absolute positions of the map peaks in Fig. 4 relative to the adopted radio position (*cross*). Low- and high-velocity components are indicated by filled and empty circles, respectively, and the corresponding radial velocities are indicated.

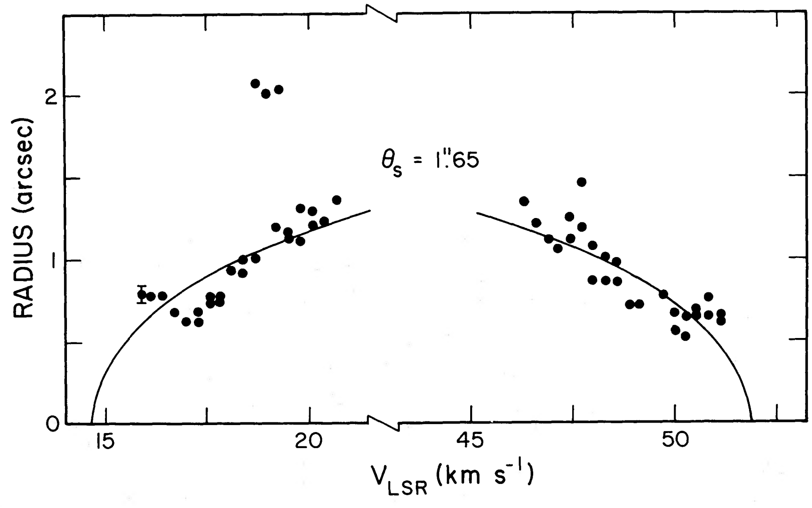

FIG. 6.—Angular distance of the map peaks from the adopted radio position of IK Tau as a function of the radial velocity. The broken curve indicates a least-squares fit of eq. (1). The error bar indicates the positional uncertainty of individual components.

1989ApJ...340..479B

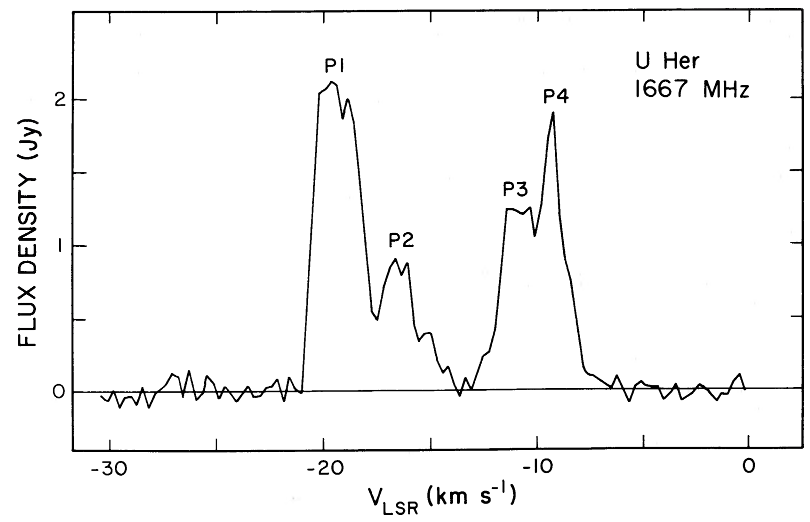

FIG. 7.—Spectral-line profile of the 1667 MHz emission from U Her

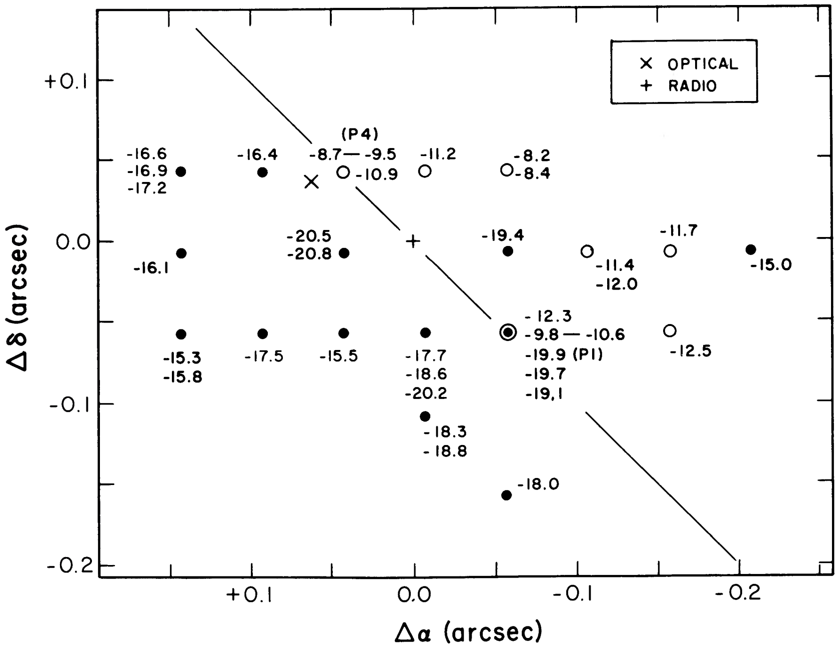

FIG. 8.—Absolute positions of the 1667 MHz emission components of U Her relative to the adopted radio position (*cross*). The optical position "x" is corrected for proper motion to the epoch of the radio data. Filled and empty circles respectively denote low- and high-velocity emission relative to V_0. The diagonal line indicates the sense of the velocity discontinuity.

are significant differences in the structure at a given velocity. At $V = 40.6$ km s^{-1} their map shows a complex distribution centered near the map origin with emission at all position angles, whereas our map shows a complex distribution located primarily south and east of the origin. At the most extreme high velocity of 54.8 km s^{-1}, our data show two unresolved knots of comparable intensity at a position angle of about $-20°$ with each knot located at least 0"5 from the map origin, whereas their map indicates a strong component at the map origin and a weak extension of emission northward at a position angle of about $+20°$. At intermediate velocities the two sets of maps agree reasonably well, if we allow for our better signal-to-noise ratio and dynamic range. The differences between the two data sets may be caused by intrinsic changes as a function of time (epoch 1980.9 vs. 1985.1), by different velocity resolutions (1.1 km s^{-1} vs. 0.3 km s^{-1}), or perhaps a combination of both.

The absolute positions of the map peaks in Figure 11 are summarized in Figure 12*a* for the low-velocity features and Figure 12*b* for the high-velocity features. The "x" and the cross, respectively, denote the optical and H_2O maser positions given by de Vegt *et al.* (1987). The empty triangle denotes the OH position derived by Bowers, Johnston, and Spencer (1983)

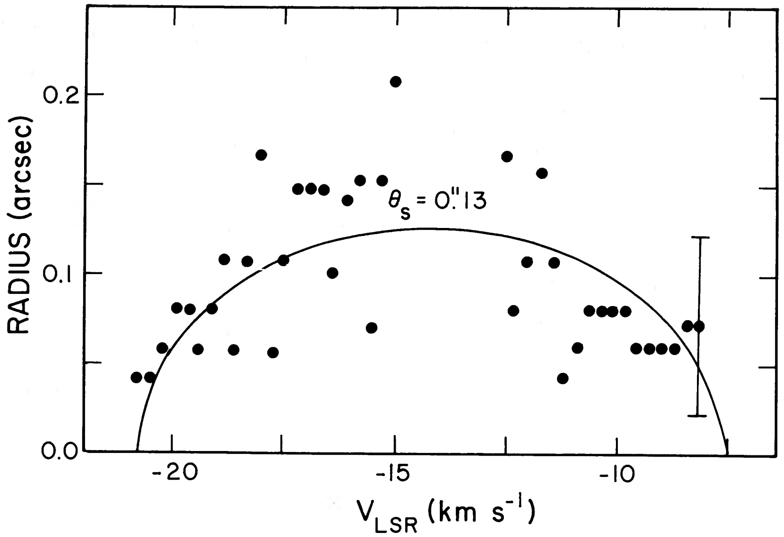

FIG. 9.—Angular distance of the emission components from our adopted radio position of U Her as a function of the radial velocity. The curve indicates a least-squares fit of eq. (1), and the error bar indicates the positional uncertainty of individual components.

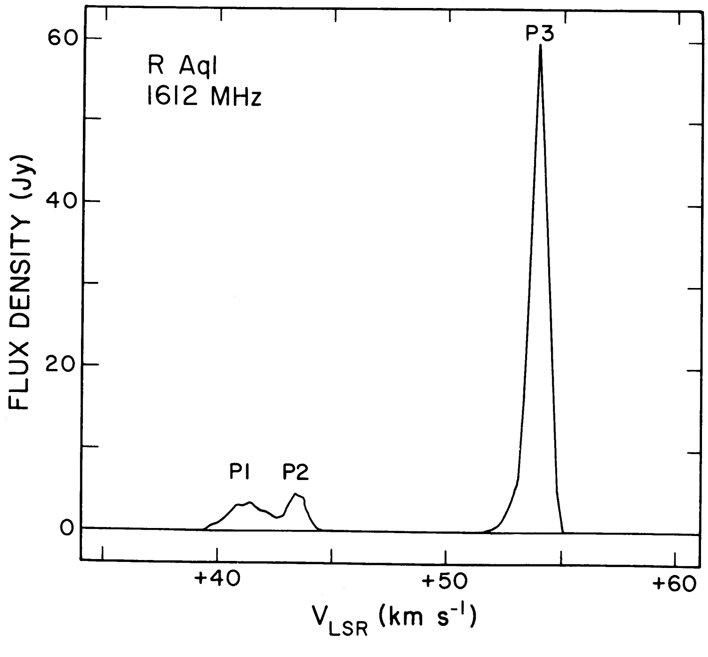

FIG. 10.—Spectral-line profile of the 1612 MHz emission from R Aql

based on positional coincidence of peak spectral features at 41.8 and 53.7 km s^{-1} in the maps of de Vegt *et al.*, and the filled triangle represents the mean position of these same features derived from the present data. At velocities where multiple peaks are evident in the maps and in the clean components, the positions of all the peaks are plotted.

It is difficult to derive an accurate OH position for this star, because the emission distributions are resolved and complex at the outer peaks and extrema in the profile. This difficulty is illustrated by the different positions of the filled and empty triangles in Figure 12. Regardless of possible temporal changes, the accuracy of the OH position can be relatively poor in complex cases, because of limitations imposed by the spatial and velocity resolutions, the spectral sensitivity, and asymmetries in the emission distributions.

Figure 12 shows that the position derived from the H_2O masers is in reasonably good agreement with the optical position; the offset of ~0".2 between the two is typical of the observed differences between the radio and optical reference frames. The distribution of H_2O masers is also complex, but they occur closer to the star and thus are distributed over a smaller angular extent. We therefore adopt the H_2O position

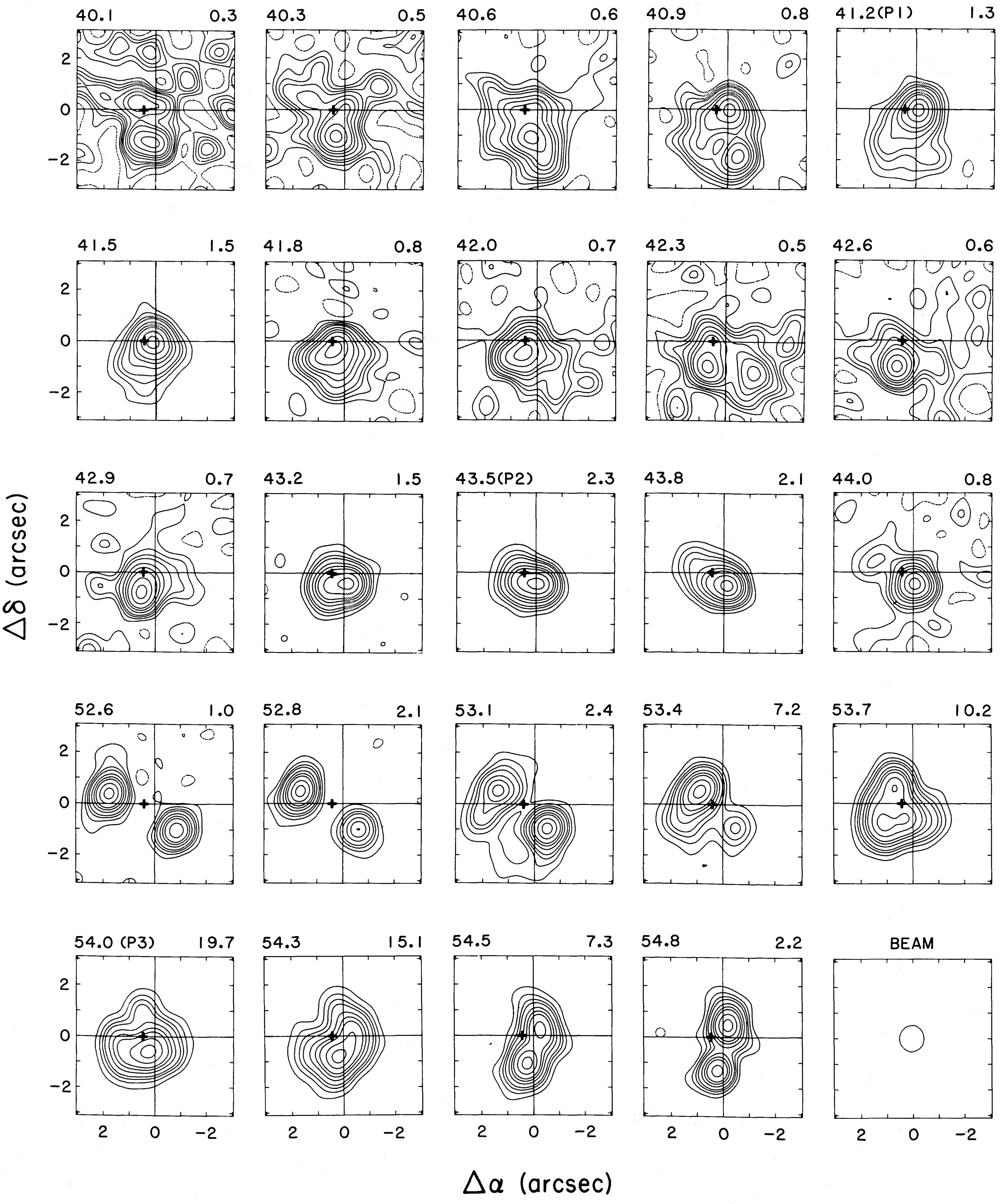

FIG. 11.—Maps of the angular distribution of emission from R Aql at 1612 MHz. The map origin corresponds to $\alpha(1950) = 19^h03^m57^s.660$, $\delta(1950) = +08°09'07''.85$. The small cross in each map represents the position of the H_2O maser emission and also our adopted radio position. Labeling of the maps is the same as for Fig. 4.

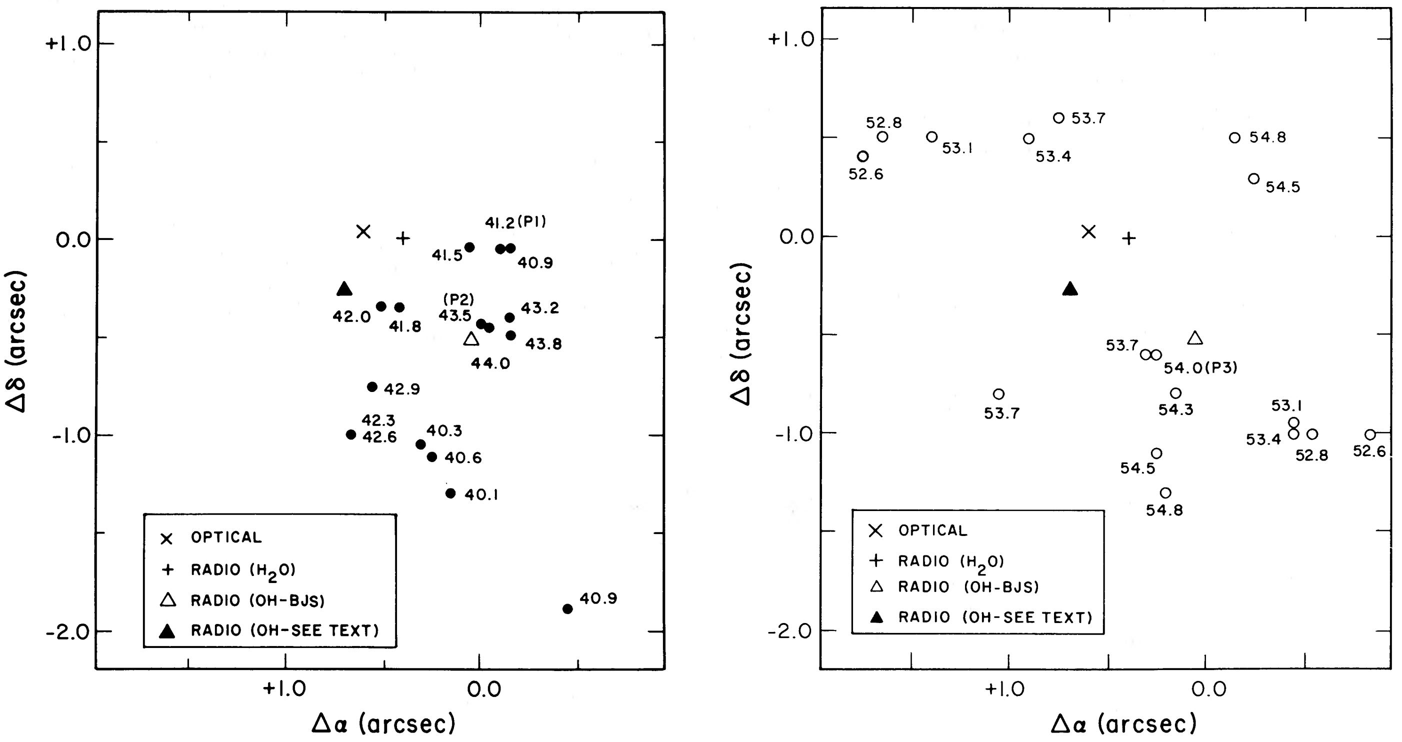

FIG. 12*a*

FIG. 12*b*

FIG. 12.—(*a*) Absolute positions of the low-velocity ($V < V_0$) map peaks of R Aql relative to the origin in Fig. 11. The "x" indicates the optical position, the cross indicates the position of the H_2O maser emission (de Vegt *et al.* 1987), the empty triangle indicates the OH position given by Bowers, Johnston, and Spencer (1983), and the filled triangle indicates the present mean position of OH features at the same velocities. All positions are corrected for proper motion to epoch 1985.11. Radial velocities are appropriately indicated. (*b*) Same as (*a*), for the high-velocity ($V > V_0$) map peaks.

as the stellar position (in the radio reference frame). The error associated with this position is about $\pm0\farcs15$ and is determined from the size of the H_2O maser region (de Vegt *et al.* 1987).

Relative to this position, the strongest low-velocity map peaks are distributed primarily between position angles of 90° and 270°. At velocities closest to V_0, both the low- and high-velocity emission show elongated structures oriented northeast by southwest. Figure 11 shows that the strong, resolved, peak spectral feature at 54.0 km s^{-1} (P3) is centered near the adopted stellar position, based on the geometric centroid at the lowest contour level.

In Figure 13 we plot the angular radius as a function of radial velocity for the map components relative to the adopted stellar position. The angular radius increases from 42.0 to 44.0 km s^{-1} and from 54.0 to 52.6 km s^{-1}, indicative of radial expansion, but there are maser components more than 1″ from the star at the extreme low and high velocities in the profile. For example, at the extreme high-velocity end of the profile ($V \geq 54.5$ km s^{-1}), the emission distribution consists of double components at $\sim0\farcs7$ and $1\farcs3$ from our adopted location for the star.

In the context of the standard model, the parabolic curves in Figure 13 define inner and outer radii between which the maser emission can originate. To produce these curves we have used equation (1) with $V_0 = 47.4$ km s^{-1} and $V_e = 8.9$ km s^{-1}. The value of V_0 is the mean velocity of the OH emission (from Fig. 10) and is midway between the values of $V_0 = 48.7$ km s^{-1} and $V_0 = 46.3$ km s^{-1}, respectively, determined by Dickinson *et al.* (1978) and by Nyman and Oloffson (1985) from the ($v = 0$, $J = 2$–1) SiO transition. The value of V_e is taken from the SiO measurement by Nyman and Oloffson and is slightly larger than the values of 7.4 km s^{-1} (from the OH profile) and 7.7 km s^{-1} (from Dickinson *et al.*). It is evident that this model does not easily explain the complex structure at the extreme velocities.

v) *RR Aql*

The profile at 1612 MHz is shown in Figure 14 and exhibits four major emission peaks labeled P1–P4 at velocities of 21.2, 22.9, 32.5, and 34.0 km s^{-1}, respectively. Maps were made of detectable features between 20.6 and 24.3 km s^{-1} and between 31.7 and 34.8 km s^{-1}, and selected maps are shown in Figure 15. The emission is unresolved at the lowest ($V < 24$ km s^{-1}) and highest ($V > 33.5$ km s^{-1}) velocities. At intermediate velocities (24.0–24.3 km s^{-1} and 31.7–33.4 km s^{-1}) the emission is slightly resolved and the size of the emission region tends to increase as the velocity approaches the midpoint of the profile in Figure 14. The extreme low- and high-velocity features (20.6 and 34.8 km s^{-1}) are offset by $0\farcs1$ in declination, and we adopt their mean position as the radio position of the star. The origin of the maps in Figure 15 is located at this position.

The absolute positions of the emission components are summarized in Figure 16. At $V = 24.3$, 31.7, 32.0, 32.8, and 33.1 km s^{-1}, the maps in Figure 15 (and the clean components) suggest at least two map peaks at each velocity, and we have plotted both positions. The cross at the map origin designates our inferred OH position of the star, and the "x" designates the optical position. The triangle denotes the H_2O position given

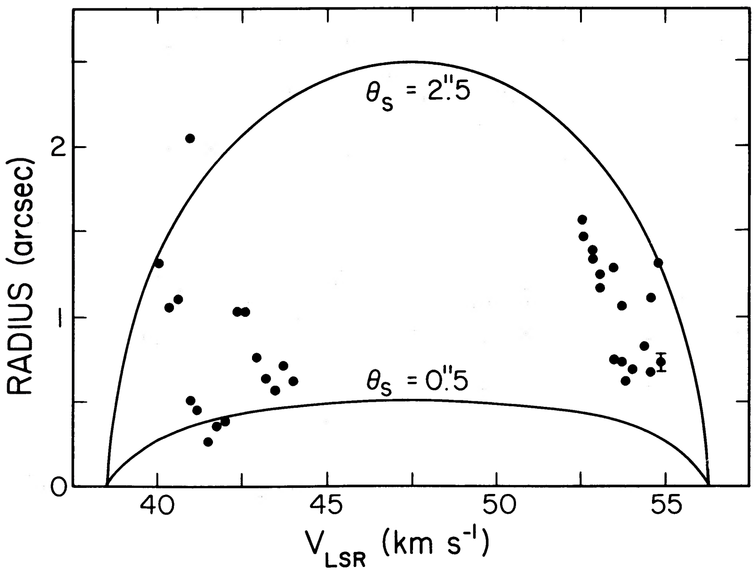

FIG. 13.—Angular distance of the 1612 MHz OH components from our adopted radio position of R Aql as a function of the radial velocity. The curves indicate inner and outer radii between which the emission is located (see text), and the error bar indicates the positional uncertainty of individual components.

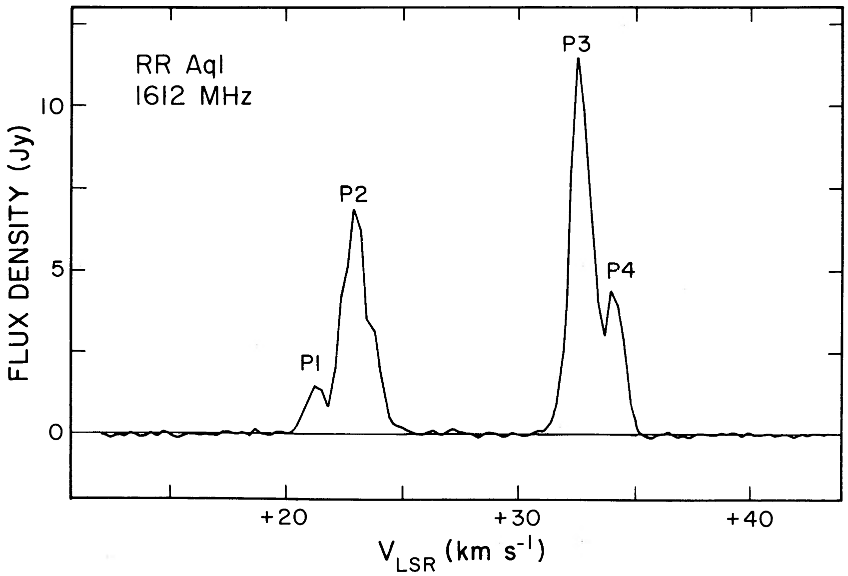

FIG. 14.—Spectral-line profile of the 1612 MHz emission from RR Aql

by de Vegt *et al.* (1987), derived from the centroid of the H_2O distribution determined by Johnston, Spencer, and Bowers (1985); it agrees to within $0\farcs02$ with our OH position.

Our inferred radio position differs by only $0\farcs05$ from the mean position of the outermost peak spectral features (P1 and P4) which are unresolved and positionally coincident to within our errors. The two OH positions given by de Vegt *et al.* differ significantly but are derived from the positions of P2 and of the mean of P2 and P3. Our OH position differs by $\sim 0\farcs4$ in declination from the OH position given by Bowers, Johnston, and Spencer (1983). They estimated their error in absolute position to be about $\pm 0\farcs3$; the slightly larger offset of $0\farcs4$ may be caused by ionospheric effects for their observations of this star. Unlike the case of R Aql, we think that temporal changes or different velocity resolutions are not as likely to explain this discrepancy because of the simple structure of the outermost spectral features.

Relative to the radio position of the star, Figures 15 and 16 show that the high-velocity ($V > 30$ km s^{-1}) components are located at all position angles, although the strongest components are southwestward of the star at an angular distance of $\sim 0\farcs5$. The low-velocity components ($V < 25$ km s^{-1}) appear to be clustered closer to the star with the majority of them also located southwestward. The angular distance from

1989ApJ...340..479B

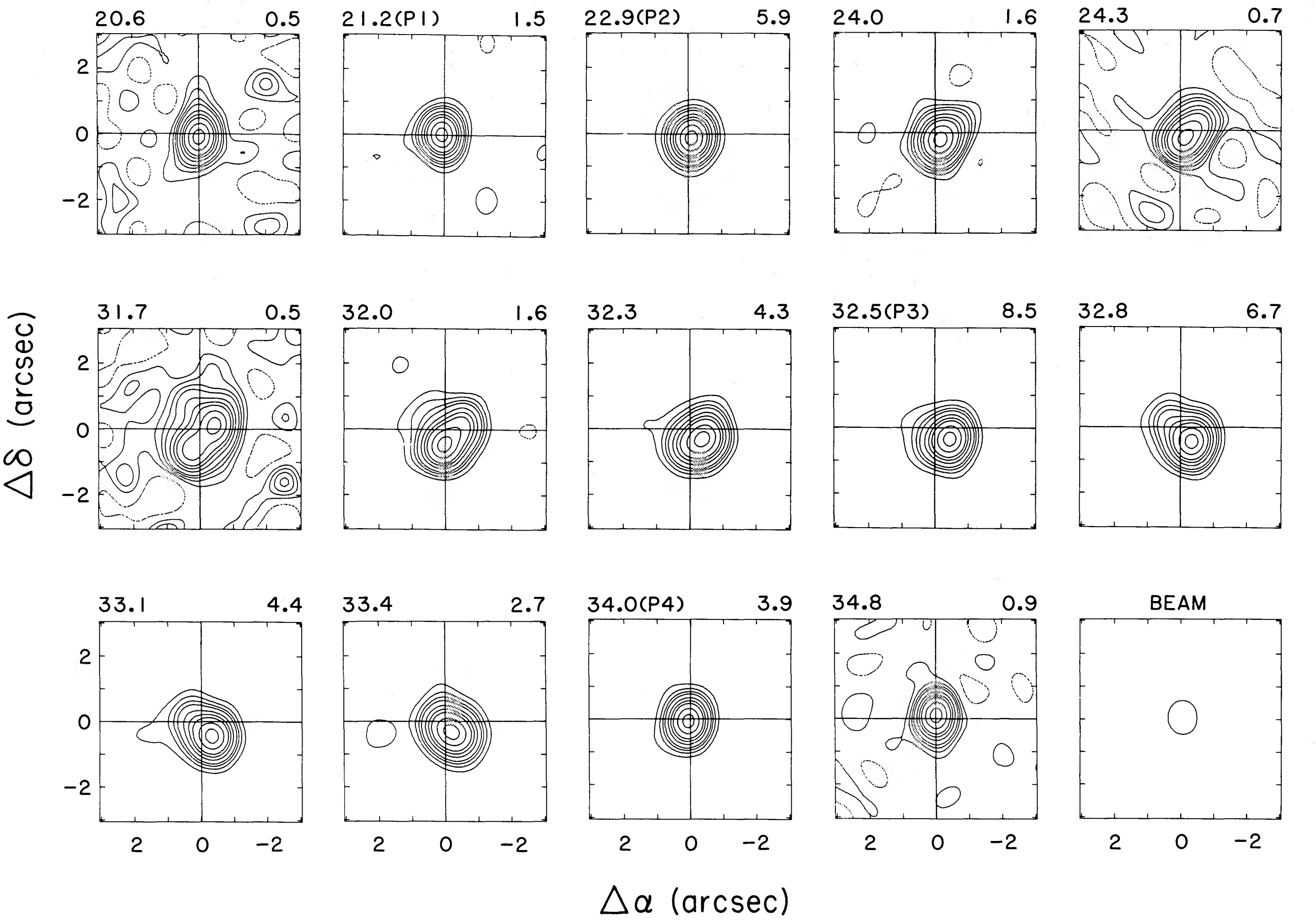

FIG. 15.—Maps of the angular distribution of emission from RR Aql at 1612 MHz relative to our adopted radio position. Labeling of the maps is the same as for Fig. 4.

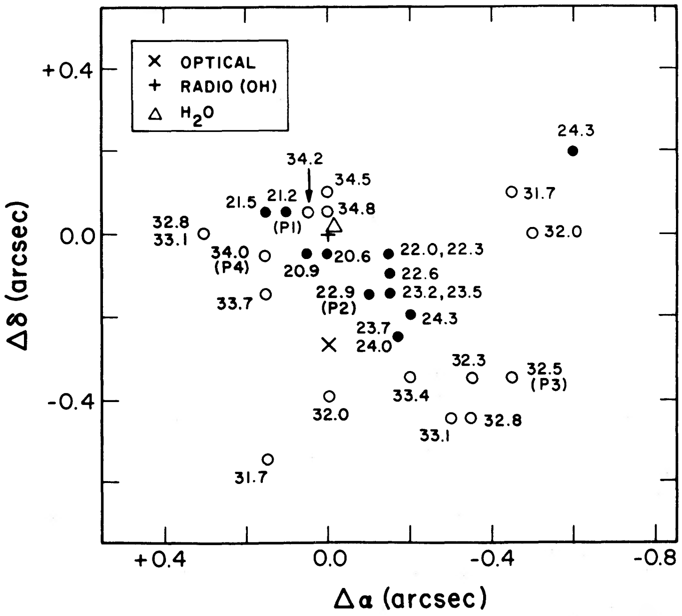

FIG. 16.—Absolute positions of the emission components of RR Aql relative to the adopted radio position (epoch 1985.11) which is indicated by the cross. The triangle denotes the position of the H_2O masers (epoch 1982.22) and the "x" denotes the optical position (epoch 1984.01). Filled circles represent low-velocity components ($V < V_0$), and empty circles represent high-velocity components ($V > V_0$).

the stellar position is plotted as a function of velocity in Figure 17, and it is evident that the radii of the near and far sides of the maser region are significantly different. A least-squares fit of equation (1) to all the data yields $V_0 = 27.8 \pm 0.1$ km s^{-1} and $V_e = 6.8 \pm 0.2$ km s^{-1}. Subsequent fits of equation (1) (with V_0 and V_e set to constants) give values of $\theta_s = 0''.30 \pm 0''.02$ and $\theta_s = 0''.59 \pm 0''.04$ for the radii of the near and far sides of the maser region; these fits are indicated by the solid curves in Figure 17. In comparison, Diamond *et al.* (1985) found an average angular radius of 0''.5 from MERLIN observations. The poorer quality of the fit for the high-velocity emission suggests either a significant distortion from constant radial expansion or a considerably thicker maser region on the far side of the envelope.

IV. STRUCTURE OF THE MASER REGIONS

The available data now provide the following constraints on a model of the OH maser regions (and envelope structures) of oxygen-rich red giants.

1. At small radii ($R \leq 50$ AU), there is an angular separation between emission at $V < V_0$ and emission at $V > V_0$. This effect is seen for the two cases which thus far have been mapped—U Ori and U Her—and we consider it to be a fundamental indication of axisymmetric structure in the maser regions. The emission is not strongly confined to a plane, however, since partial ringlike structures are seen for U Ori. The $\theta(V)$ relationships provide definite evidence for radial expansion in these small shells, but the profiles show complex, multiply peaked structures which are not expected from the standard model.

2. At intermediate radii ($100 \leq R \leq 500$ AU), there also are indications of axisymmetric structure, particularly at velocities closest to the stellar velocity. Specifically, emission at these velocities tends to be located along an axis on the sky which passes through the stellar position. The velocity-integrated emission distribution may show gas at all position angles relative to the star, but it tends to be elongated along the same axis.

At the extreme low and high OH velocities, the map features may be complex and displaced from the stellar position, yielding nonzero values of θ in contradiction to the prediction of the standard model. At other velocities, multiple values of θ may occur at a given V. Profiles typically show multiply peaked structures concentrated in two velocity ranges.

3. At large radii ($R > 500$ AU) characteristic of OH/IR stars, the emission is distributed in clumpy, approximately circular rings centered on the star without clear indications of axisymmetric structures. The size of the rings usually increases as $V \rightarrow V_0$, in accordance with equation (1), but complex emission structures at the extreme low or high velocities are sometimes present, resulting in nonzero values of θ at these velocities. Statistically, the profile shapes approach that which is expected in the standard model (see Johansson *et al.* 1977). Examples of the map distributions for a number of these stars are given by Bowers, Johnston, and Spencer (1983), Herman *et al.* (1985), and Welty, Fix, and Mutel (1987).

These constraints suggest a model in which an axisymmetric configuration of the OH is evident at small shell radii but the configuration tends toward a spherical distribution at large radii with radial expansion at a constant velocity. We present such a model in § IV*b*. Before doing so, we consider in more detail the velocity structure at small distances from the star (§ IV*a*). In particular, we examine whether significant acceleration, rotation, or velocity fluctuations are present in the inner envelope, since this is of importance for determining the uniqueness of the model.

a) Velocity Structure

i) *Acceleration*

The standard model predicts little radial acceleration at $R > 10^{16}$ cm (e.g., Goldreich and Scoville 1976). At smaller radii significant acceleration has been suggested by several authors. Perhaps the most direct evidence is given by Chapman and Cohen (1986), who measured the radii and outflow velocities of SiO, H_2O, and OH masers for the supergiant VX Sgr. They find $\epsilon \approx 1$ at $R \approx 50$ AU, $\epsilon \approx 0.5$ at 200 AU, and $\epsilon \approx 0.2$ at 1300 AU, where $\epsilon = (d \ln v)/(d \ln r)$. Arguments for acceleration at $R \leq 10^{15}$ cm also have been made by Bujarrabal *et al.* (1986) to account for narrow line shapes of thermal SiO profiles of Mira variables and by Nguyen-Q-Rieu

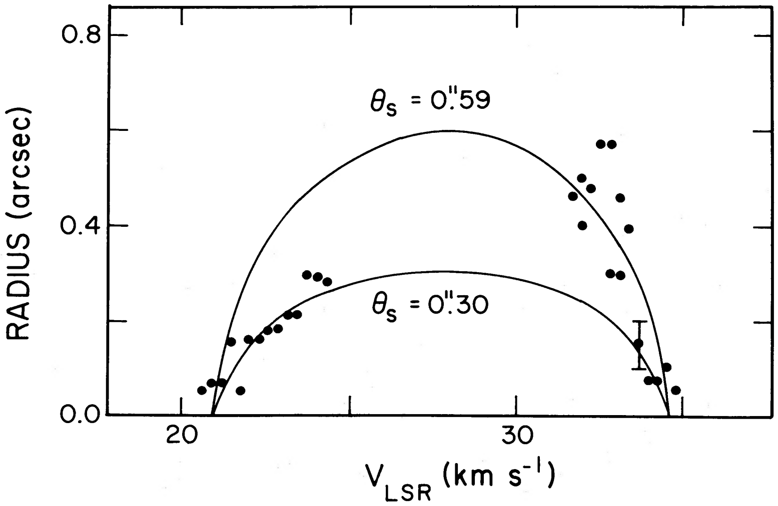

FIG. 17.—Angular distance of the 1612 MHz map peaks from our adopted radio position for RR Aql as a function of the radial velocity. The curves indicate separate least-squares fits to the low- or high-velocity data. The error bar indicates the positional uncertainty of individual components.

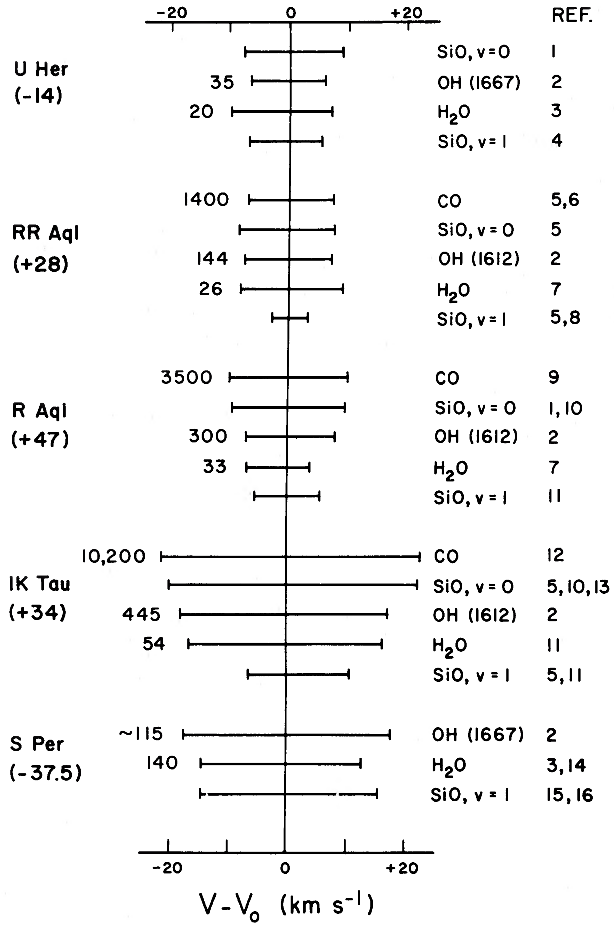

FIG. 18.—Largest velocity ranges observed for OH, H_2O, SiO, and CO, and estimated radii (AU) of the corresponding shells. Parenthetic values under the star names are the adopted stellar radial velocities V_0. References are as follows: (1) Morris *et al.* 1979. (2) This paper. (3) Engels, Schmid-Burgk, and Walmsley 1988. (4) Jewell *et al.* 1987. (5) Bujarrabal *et al.* 1986. (6) Zuckerman and Dyck 1986. (7) Johnston, Spencer, and Bowers 1985. (8) Snyder and Buhl 1975. (9) Wannier and Sahai 1986. (10) Nyman and Olofsson 1985. (11) Nyman and Olofsson 1986. (12) Knapp and Morris 1985. (13) Nguyen-Q-Rieu *et al.* 1988. (14) Diamond *et al.* 1987. (15) Kaifu, Buhl, and Snyder 1975. (16) Spencer *et al.* 1981.

et al. (1979) to account for maser emission at velocities outside the range defined by the doubly peaked emission structures.

To investigate the possibility of significant acceleration in the OH maser regions, we summarize in Figure 18 the available molecular line data pertinent to the velocity structure of the envelopes. For each transition we plot the minimum and maximum velocities relative to V_0 thus far published in the literature. We find that values of V_0 determined from OH agree to within the observational errors (2 km s^{-1}) with those determined from high-quality, thermal SiO or CO profiles. For one case (S Per) the difference is larger (5 km s^{-1}), but Morris *et al.* (1979) indicate that the SiO detection is at the 2 σ level. We have not plotted their data on Figure 18. Our best estimate of V_0 is listed under the star's name and is based on all three of these species; we estimate the accuracy to be about ± 1 km s^{-1}.

For each star the velocity ranges are plotted from bottom to top in approximate order of increasing radius of the emission region. The numbers to the immediate left of the velocity ranges indicate observational (H_2O and OH) or theoretical (CO) estimates of the radii. For H_2O we compute R from one-half the angular size given in Table 5. For CO we compute R to be the photodissociation radius, using the model of Mamon, Glassgold, and Huggins (1988) and the values of $\dot{M}$ and V_e in Table 4. The Mira stars have been arranged in order of increasing mass loss rate (from top to bottom). This is also the order of increasing expansion velocity (as measured from the thermal lines) and of increasing H_2O, OH, and CO shell radii.

It is well known that H_2O and ($v = 1$) SiO maser emission is highly variable with time. However, there are now numerous observations of this emission at different epochs, increasing the probability that the lowest and highest velocities have been sampled and that comparison to other species is meaningful. This is supported in a few cases by approximate symmetry of the velocity ranges relative to the values of V_0 inferred from OH and the thermal lines.

Figure 18 shows several interesting results:

1. The values of V_e indicated by high-quality CO and thermal SiO profiles agree to within 2 km s^{-1} for the three stars where both lines have been detected, suggesting that the emission from both these species is distributed into regions where the velocity field is similar and probably is almost entirely constant radial expansion.

2. The velocity range of OH is less than those of the thermal lines in all cases, suggesting a net radial acceleration in the

TABLE 6

Derived Velocity Gradients

	$(H_2O - OH)$		$(OH - CO)$	
Star	Radius (AU)	ϵ	Radius (AU)	ϵ
U Her	20–35	-0.77	...	
RR Aql	26–144	-0.11	144–1400	0.00
R Aql	33–300	$+0.06$	300–3500	$+0.09$
IK Tau	54–445	$+0.04$	445–10200	$+0.07$
S Per	140–115	-0.96[a]	...	

[a] Inferred radii of H_2O and OH regions are equal to within the respective errors.

outer envelope. We summarize in Table 6 the values of ϵ derived among the H_2O, OH, and CO regions. In no case do the data indicate values larger than 0.1 in the OH shells of Mira variables. Such a small value of ϵ has little effect on the OH profile shapes or angular distributions.

3. The H_2O masers occur at velocities outside the range of the thermal SiO and CO for U Her and RR Aql. This may suggest significant turbulent motions or rotation in the smaller H_2O shells or different geometric distributions (§ IV*b*).

4. The SiO masers occur at velocities comparable to or less than the H_2O masers. Since the SiO masers are yet closer to the star where thermal or turbulent motions are expected to be greater, this result suggests that the radial expansion may be initiated at radii between the likely location of the SiO masers and the H_2O masers, consistent with the formation of dust between these two maser regions (Dyck *et al.* 1984). Again, different geometric distributions can complicate the interpretation.

ii) *Rotation*

In view of the axisymmetric geometries indicated by the data, it is important to examine the possible role of rotation. Significant rotation is not expected at large distances from the star (e.g., Wilson, Barrett, and Moran 1970), but it has been suggested as a means to account for profile shapes of SiO maser emission for some stars (Van Blerkom and Auer 1976; Van Blerkom 1978; Zhou Zhen-pu and Kaifu 1984). We therefore consider a velocity field consisting of both radial expansion and Keplerian rotation.

The velocity field is illustrated in Figure 19. We assume that the OH is uniformly distributed in an annular region whose plane is edge-on to the line of sight. The radial component $V_{\rm rad}$ and the tangential component $V_{\rm tan}$ have equal velocities of 7.07 km $\rm s^{-1}$ at the inner shell radius R_i (i.e., $V_{\rm total}$ is 10 km $\rm s^{-1}$). $V_{\rm rad}$ is constant at all radii and $V_{\rm tan} \propto R^{-0.5}$, although the value of the exponent is of little importance for thin shells. We adopt $R_0/R_i = 2$ (Table 4). The contours indicate the line-of-sight radial velocity V as viewed from the Earth when the stellar velocity is 0 km $\rm s^{-1}$. Amplification occurs along the line of sight only so long as $|V \pm \Delta V| < V_D/2$, where V_D is the Doppler width. The resulting $\theta(V)$ relationship is shown in Figure 20, where $\theta_{\rm max}$ is the maximum possible angular shell radius and θ is the predicted angular radius of the maximum velocity-coherent path-length at a given V. We take $V_D = 2.0$ km $\rm s^{-1}$ to compute these curves, implying $T \approx 1000$ K. Different values of V_D produce changes near the extreme velocities which are small and not significant for the present discussion. To facilitate comparison of Figures 19 and 20, we indicate with the solid curve those values of θ for which the velocity-coherent path length is longer. We have computed model angular distributions, $\theta(V)$ relationships, and profile shapes for a wide range of input parameters. The model in Figures 19 and 20 is adequate to illustrate the salient characteristics expected in the data.

Figure 20 shows that the $\theta(V)$ relationship is double-valued and has a complex shape with nonzero values at the extreme low and high velocities. These effects are also easily seen in Figure 19. If $V_{\rm tan} = 0$, the curves in Figure 20 degenerate into the parabolic relationship of equation (1). As $V_{\rm tan}/V_{\rm rad}$ increases, the separation of the maxima increases and the separation of the zero points decreases. Thus, depending on the ratio $V_{\rm tan}/V_{\rm rad}$, a wide range of angular distributions [and $\theta(V)$

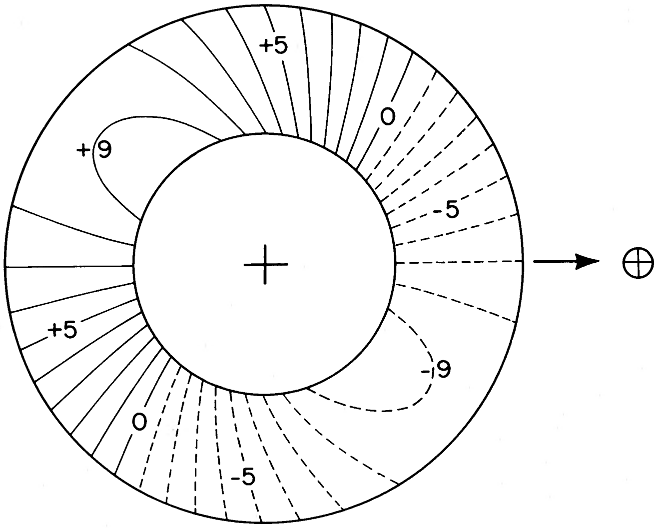

Fig. 19.—Model of the velocity field for an edge-on disk in the case where the radial and tangential components have equal values of 7.07 km $\rm s^{-1}$ at the inner radius of the annulus. The dashed and solid contours indicate the line-of-sight radial velocities relative to the stellar velocity. OH is assumed to be uniformly distributed in the annular region of thickness $R_0/R_i = 2$.

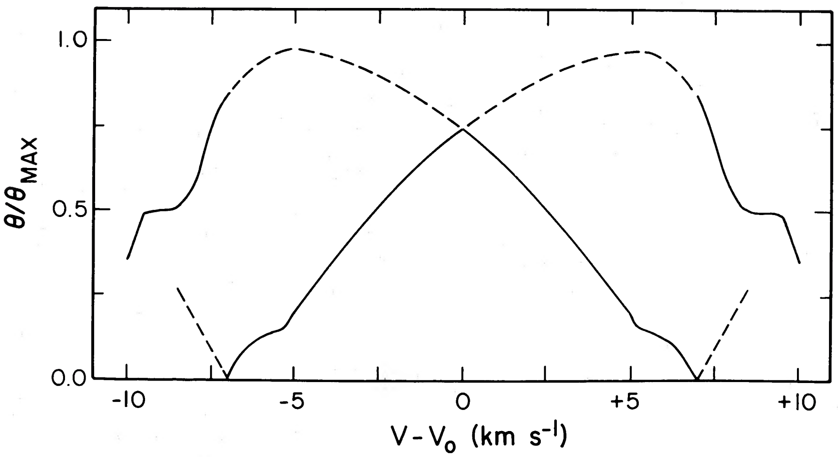

FIG. 20.—$\theta(V)$ relationship for the model in Fig. 19, where the angular radius θ is normalized to the maximum possible shell radius. The solid curve indicates those values of θ for which the velocity-coherent path length is longer.

relationships] is possible. Further complications are introduced at high latitudes from the plane of rotation where the velocity field will tend toward constant radial expansion.

Is there evidence for rotation in the OH shells? For U Ori, Bowers and Johnston (1988) place an upper limit of ~3 km s^{-1} on any line-of-sight rotation, giving $V_{tan}/V_{rad} \leq 40\%$ in their model. That limit was obtained by comparing curves such as those in Figure 20 to the data and allowing for the observational errors. For U Her, the errors are larger in relation to the shell size θ_s, but comparison of Figure 20 to Figure 9 clearly indicates that $V_{tan} < V_{rad}$. The upper limit to any line-of-sight rotation is ~4 km s^{-1} ($V_{tan}/V_{rad} \leq 70\%$) if the OH is uniformly distributed throughout the annulus. Thus there is no evidence that rotation dominates the motion in the smallest shells.

For IK Tau and R Aql, the nonzero values of $\theta(V)$ at the extreme low and high velocities might suggest a model with $V_{tan} > V_{rad}$. We think this unlikely, though, since we expect less evidence for rotation in these larger shells. The map structures also are difficult to explain with this model. For example, if the plane of rotation for R Aql is oriented NE-SW, as suggested by the maps at 44 and 53 km s^{-1} in Figure 11, it is difficult to explain the emission southward of the star at the extreme low (40.1–41.2 km s^{-1}) and high (54.0–54.8 km s^{-1}) velocities where we expect the emission to lie in the plane. Alternatively, if the plane is oriented NW-SE, it is difficult to understand the complex structure at 54.8 km s^{-1} which is not predicted by a rotational model.

We cannot unequivocally rule out the possibility of a rotational component in some of the envelopes, but the data appear to indicate that rotation is not a *primary* kinematic component in the OH shells of Mira variables.

iii) *Velocity Fluctuations*

Random velocity fluctuations (or streaming motions) can account for some complexities in profile shapes and angular distributions (Deguchi 1982). Values of ~2 km s^{-1} or less (comparable to the sound speed) have been estimated for OH/IR stars (Bowers, Johnston, and Spencer 1983; Diamond *et al.* 1985). For values of this magnitude, the velocity fluctuation model predicts that extreme velocity features have only small angular displacements ($\theta/\theta_s < 10\%$) from the stellar position. The values of θ/θ_s for IK Tau (Fig. 6) and R Aql (Fig. 13) are much larger than this and also larger than those for U Her (Fig. 9) and RR Aql (Fig. 17). Thus this model would require larger motions in larger shells, contrary to previous results and to theoretical constraints. It is likely that velocity fluctuations are present in the envelopes, but they introduce a randomness onto predicted relationships and cannot be used to explain systematic effects such as axisymmetric structures.

b) Spatial Structure

In § IV*a* we conclude that the influences of radial acceleration, rotation, or random velocity fluctuations are not adequate to explain the effects seen in the data in a self-consistent manner and that the primary kinematic component must be radial expansion at a nearly constant velocity, even at radii as small as 50 AU. We now consider an axisymmetric (ellipsoidal) distribution of the material. This type of geometry previously has been considered by Jura (1983) in an effort to understand its effects on estimates of the mass-loss rates of objects with bipolar outflows. Here we examine its effects as they pertain to the observed angular distributions and profile structures of the maser emission. For simplicity (and brevity) we discuss the case where the outflow velocity has a constant value of 10 km s^{-1} in all directions, although we note that more complicated velocity fields in which the outflow velocity varies with latitude from the equatorial plane are not ruled out by the constraints established in § IV*a*.

The model is shown in Figure 21 for the case where the equatorial plane is inclined to the line of sight by 45°. Mass loss occurs in all directions relative to the star with a total density distribution which decreases as the latitude $|\lambda|$ from the equatorial plane increases. The OH is produced primarily by photodissociation of H_2O due to ambient ultraviolet radiation (Goldreich and Scoville 1976; Huggins and Glassgold 1982; Netzer and Knapp 1987), and the maser emission (if present) is confined between the indicated annuli, with a smaller radius along the polar axis[4] because there is less attenuation of UV radiation in this direction (Jura 1983). We assume that the radial thickness between the annuli is approximately constant in all directions ($R_0/R_i \approx 2$ along the polar axis), and, for the

---

[4] The term "polar axis" is here defined relative to the equatorial plane and differs from the usage of Bowers and Johnston (1988).

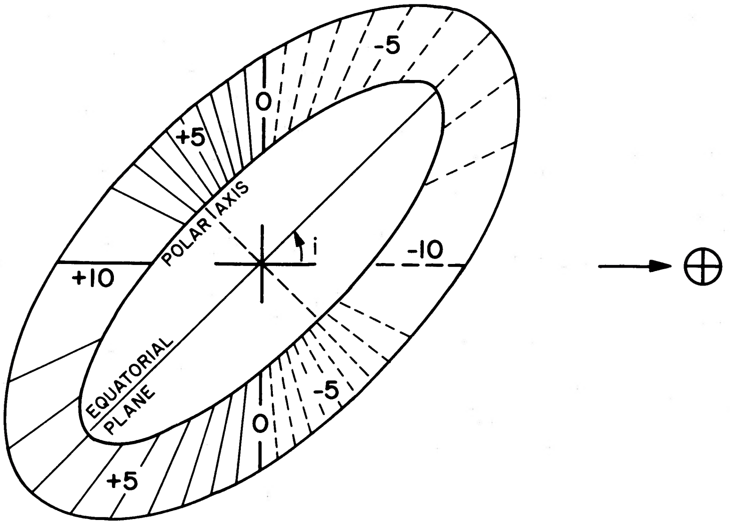

FIG. 21.—Proposed model for the structure of circumstellar OH shells. The envelope structure is a radially expanding ellipsoid whose equatorial plane is inclined to the line of sight by the angle *i*. The OH (if present) is confined between the indicated annuli. The outflow velocity is assumed to be 10 km s^{-1} in all directions, and the lines connecting the inner and outer radii of the annular region indicate the line-of-sight radial velocities relative to the stellar velocity. A large ellipticity ($e = 0.866$) is assumed for the purpose of illustration.

purpose of illustration, we assume a large ellipticity of $e = 0.866$ ($R_{\rm pol}/R_{\rm eq} = 0.5$ as measured from the outer radii). The contour lines in the figure indicate the radial velocities observed from the Earth.

The observed angular distribution depends on the degree of saturation of the emission and on the spatial uniformity of the OH. If the pump rate and OH density are constant at all latitudes, the output flux density S is proportional to the line-of-sight, velocity-coherent path length L for saturated emission ($S \propto e^L$ for unsaturated emission), so stronger emission will tend to be located in regions where L is larger. If the emission is unsaturated, Figure 21 indicates that we will see an angular separation of low- and high-velocity features on the plane of the sky, lying along the projected polar axis. If the emission is fully saturated, we will see an asymmetric ring structure at a given velocity with a nonuniform brightness distribution, as is frequently the case for OH/IR stars. Thus the tendency for axisymmetric structure to be more evident in the small OH shells of stars with low mass-loss rates (e.g., U Ori and U Her) can be explained, in part, by a smaller degree of saturation for the emission.

Spatial nonuniformity of the OH in the smaller envelopes may also contribute to this effect. If the mass distribution is anisotropic, there is a latitudinal dependence of the attenuation of the UV radiation, so the OH may be more abundant at the higher latitudes. For a given mass-loss rate, the OH would then become more uniformly distributed in larger (rarefied) envelopes where the UV radiation can effectively photodissociate the H_2O molecules at all latitudes. Thus the observed OH distribution in smaller shells will again tend to lie along the projected polar axis, whereas it will be present at all position angles in larger shells.

If the H_2O masers are collisionally pumped and originate from the denser portions of the envelope (Cooke and Elitzur 1985), then the strongest H_2O masers should be located in the equatorial plane. For cases where axisymmetric structure is

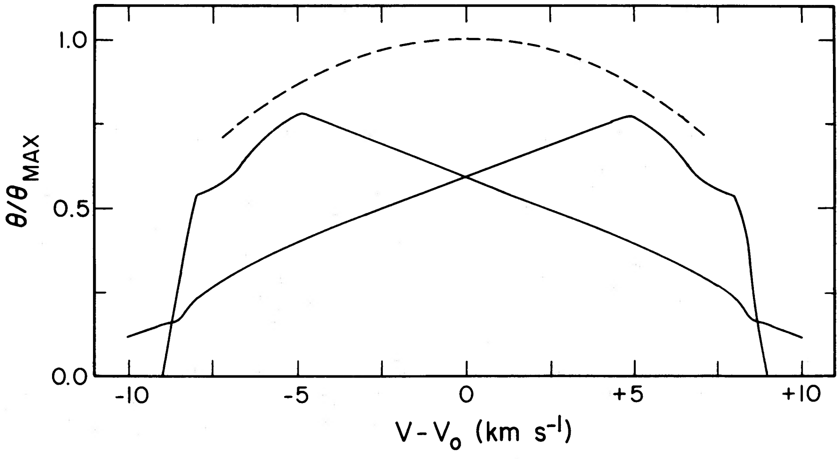

FIG. 22.—$\theta(V)$ relationship at three position angles on the sky for the configuration shown in Fig. 21. The dashed curve gives the relationship for OH located in the equatorial plane (perpendicular to the plane of the figure), and the solid curves indicate the relationships for OH emission which arises along the projected polar axis (i.e., in the plane of the figure).

1989ApJ...340..479B

seen in both the OH and H_2O distributions, we therefore expect the OH distribution to be oriented parallel to that of the H_2O masers at the extreme low and high radial velocities of the H_2O masers (e.g., IK Tau) and perpendicular to that of the H_2O masers at intermediate velocities (Table 5). At most inclinations, strong confinement of the H_2O masers to the plane also will result in a velocity range which is comparable to or less than that of the OH masers, as is generally observed to be the case (Engels, Schmid-Burgk, and Walmsley 1988). Exceptions may occur if the inclination is small and the OH is distributed only at high latitudes.

In Figure 22 we plot the $\theta(V)$ relationship derived from Figure 21, where θ is normalized to the maximum possible angular radius of the OH distribution and where we again assume a Doppler width of 2.0 km s^{-1}. The dashed curve indicates the relationship for OH in the tilted equatorial plane, and the solid curves show the relation for emission located at $|\lambda| > 0°$. It is evident that this relationship can be complex at intermediate inclinations. The solid curves closely resemble the curves for a rotating, expanding disk (Fig. 20). Figure 22 demonstrates how the angular radius θ at a given velocity depends on the position angle on the sky, giving the appearance of multiple shells in this type of plot. Inspection of Figures 21 and 22 also indicates that the angular distribution can be complex near the most extreme radial velocities, with a nonzero value of θ. This result applies even though we have assumed no random velocity fluctuations (§ IV*a*[iii]) or density clumping (e.g., Alcock and Ross 1986). The observed distribution at these velocities is a sensitive function of the assumed velocity field and the Doppler width.

In Figure 23 we show the spectral line profiles for three inclinations of the equatorial plane. The profiles have been calculated as follows (also see Bowers and Johnston 1988). The relative number of photons at velocity $V \pm V_D/2$ along a given line of sight defined by impact parameter p is

$$N_{vp} = W(L - fL_{max}) ,$$

where W is a weighting constant at velocity V, L_{max} is the maximum velocity-coherent path length at any velocity, and fL_{max} represents a threshold value of the OH column density below which there is no maser gain (e.g., Sun and Kwok 1987) and above which it is assumed that the emission is fully saturated. The line profile is then found by summation over all lines of sight through the shell: viz,

$$N_v = \Sigma_p N_{vp} .$$

A wide variety of profile shapes is possible, depending on the ellipticity, the inclination, the degrees of spatial uniformity and saturation of the OH emission, and the assumed velocity field. For the profiles in Figure 23, $W = 1$ at all velocities and $f = 0.65$. The profile shape is computed only for the two-dimensional OH distribution (in the plane of the paper; see Fig. 21).

Figure 23 shows that the profile is predominantly doubly peaked for all inclinations if the OH is uniformly distributed throughout the annular region. However, if i is not 0° and if e and f are suitably large, secondary inner peaks are produced from gas in the tilted equatorial plane because the ellipticity of the distribution promotes relatively large values of L at these velocities (Fig. 21). Such peaks are commonly seen in OH profiles, U Her being a notable example (Fig. 7). As the inclination increases, the velocity separation of the inner peaks decreases. Thus at $i = 90°$, a central peak is present at the stellar velocity, yielding a triply peaked profile. Single-peaked profiles (with the peak at $V = V_0$) also are possible if the OH is preferentially distributed at high latitudes and $i \approx 0°$. Examples of singly and triply peaked profiles can be found in the paper by Ukita and LeSqueren (1984).

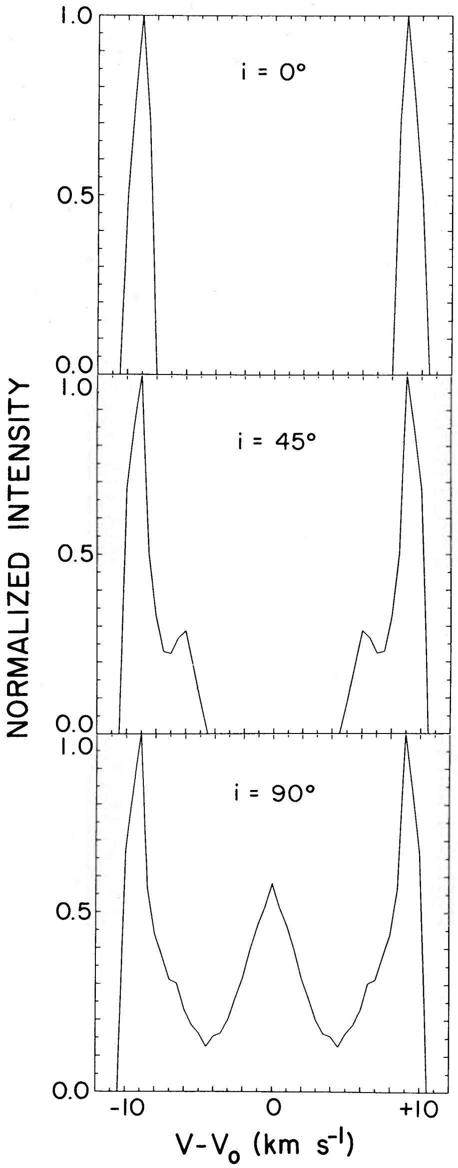

FIG. 23.—Calculated profiles for three inclinations of the ellipsoid in the case where the minimum allowed value of the velocity-coherent pathlength at a given velocity is 0.65 times the maximum value at any velocity.

In summary, the assumption of a radially expanding, ellipsoidal envelope structure provides a relatively simple way to explain numerous complexities seen in the angular distributions and profiles of circumstellar OH masers. Unfortunately, the ellipsoidal model also introduces a number of variables which are not well determined by the present data. Our computer experiments indicate that the latitudinal variation of the outflow velocity is particularly important for relating the

1989ApJ...340..479B

angular and spatial distributions of the maser emission, and further theoretical and observational efforts are needed to provide better constraints on this parameter.

V. GEOMETRY AND NATURE OF THE MASS-LOSS PROCESS

Of the six stars discussed in this paper, all but RR Aql provide evidence of axisymmetric structure in their envelopes, suggesting that this structure is common for red giant stars. The commonality is supported by recent studies of the morphologies of planetary nebulae. Zuckerman and Aller (1986) find that ~50% of planetary nebulae have bipolar structure and an additional 30% have elliptical structure. Other authors (Kahn and West 1985; Balick 1987) conclude that the morphologies of the nebulae are consistent with their formation by interacting winds (see Kwok, Purton, and Fitzgerald 1978; Kwok 1987), provided that the red giant envelopes of aspherical planetary nebulae are expelled with a lower density along their poles than along their equators. It appears, therefore, that spherical outflow from red giant stars may well be the exception rather than the rule.

Previous efforts to understand the gross structure of red giant envelopes have been hindered by the perplexing tendency for axisymmetric structure to be seen on small scales but not on large scales (Morris 1987; Dyck 1987). The results of this paper show that this tendency is also seen from the OH maser observations of optical Miras and OH/IR stars. Axisymmetric structure at large radii ($\geq 10^{16}$ cm) generally appears to be more evident among OH supergiants (§ I), suggesting that the circumstellar material for these stars is perhaps more strongly confined to a plane than is the case for red giants. We note that Zuckerman and Gatley (1988) find a trend for bipolar planetary nebulae to be associated with more massive progenitors, suggesting that the degree of axisymmetry may be related to the stellar mass (or gravity; see below).

The most likely explanation for axisymmetric geometries in the majority of late-type stars appears to be the influence of magnetic fields on the outflow. Rotation does not appear to dominate the velocity field in the inner envelopes (§ IV*a*), and the stars discussed in this paper are not known to be binaries, although close binaries may account for some axisymmetric envelopes such as that of OH 231.8+4.2 (see Morris 1987). There is, however, evidence for strong magnetic fields associated with these stars. Barvanis, McIntosh, and Predmore (1987) derive field strengths of 10–100 G for several red giant and supergiant stars based on observations of SiO masers. These values are much larger than the estimated value (0.1 G) needed for magnetic energy to dominate the gas motion. Their results are consistent with the photospheric field strengths inferred from polarized OH masers in circumstellar shells (Reid *et al.* 1979; Claussen and Fix 1982; Chapman and Cohen 1986; Cohen *et al.* 1987).

Such large field strengths make models of mass loss driven by Alfvén waves extremely relevant. Hartmann and MacGregor (1980) indicate that this mechanism can produce the mass-loss rates and outflow velocities observed for late-type stars if the field strength is ~10 G, although the mechanism is subject to a very narrow range of damping lengths (Holzer, Flå, and Leer 1983; Holzer and MacGregor 1985). Nonetheless, Hartmann and MacGregor predict that for a fixed field strength the mass-loss rate increases as the stellar gravity decreases, consistent with results which indicate higher mass-loss rates for OH supergiants than for Miras and OH/IR stars (e.g., Bowers 1981; Netzer and Knapp 1987).

No single mechanism probably can account completely for the observed properties of mass loss in cool stars (e.g., Holzer and MacGregor 1985; Willson 1987; Morris 1987), but it now seems very likely that magnetic fields are important not only for determining the geometry of mass loss but also for the role they play in initiating the mass-loss process.

VI. CONCLUSION

Our observations of optically identified Mira variables indicate clear evidence for axisymmetric structure of the OH shells at distances between ~35 and 500 AU from the star. In contrast, observations of red giants with higher mass-loss rates (i.e., OH/IR stars) indicate ring structures at radii ≥1000 AU, indicative of roughly spherical OH distributions. We find no strong evidence for radial acceleration (i.e., $\epsilon \leq 0.1$) or rotation ($V_{\rm tan}/V_{\rm rad} \leq 0.7$), suggesting that the gas is radially expanding at a nearly constant velocity even at radii as small as 35 AU. We consider the case of a radially expanding, ellipsoidal envelope structure in which material is shed off of the star in all directions with a total gas (and dust) density which varies with latitude from a plane of maximum density. This model can explain pronounced axisymmetric structure in small shells, asymmetric ring structures in larger shells, complex $\theta(V)$ relationships, and multiply peaked profile structures, none of which is predicted in the standard expanding spherical shell model. We suggest that this geometry is common for red giants (and supergiants) and is probably the result of the large magnetic field strengths which are known to exist in these stars. The higher mass-loss rates of OH supergiant stars may indicate the importance of Alfvén waves for the initiation of the mass-loss process.

The variables in this model (ellipticity, inclination, degrees of spatial nonuniformity and of saturation of the emission, and latitudinal dependence of the outflow velocity) along with random effects (velocity fluctuations, density clumping) compromise the accuracy to which the stellar position, stellar radial velocity, outflow velocity, and shell radius can be deduced. We find no method to determine the latter quantities from OH emission which is completely reliable for all cases. In general, these quantities are best determined by least-squares fitting to the $\theta(V)$ relationship, but this method requires high-quality data over a significant velocity range. Values of position, V_0, and V_e derived from the averages of the extreme low- and high-velocity features usually show good agreement ($\pm 0\rlap{.}''05$; ± 1 km s^{-1}) with the least-squares method if these features are unresolved and positionally coincident. Neither method is foolproof if there are strong asymmetries in the velocity range (e.g., U Ori) or complex angular distributions (e.g., R Aql). If the emission distribution is strongly aspherical, derived values of the outflow velocity and shell radius also may be less than the maximum values in the envelope.

We thank the National Radio Astronomy Observatory for providing observing time for this project and the Astronomical Rechen Institut in Heidelburg for making available the FK 5 data in advance of publication. C. d. V. thanks the Bundesministerium für Forschung und Technologie (BMFT) for financial support under grant No. 100013-8 (HIPPARCHOS).

REFERENCES

Alcock, C., and Ross, R. R. 1986, *Ap. J.*, **305**, 837.
Balick, B. 1987, *A.J.*, **94**, 671.
Barvanis, R., McIntosh, G., and Predmore, C. R. 1987, *Nature*, **329**, 613.
Baud, B. 1981, *Ap. J.* (*Letters*), **250**, L79.
Baudry, A., LeSqueren, A. M., and Lépine, J. R. D. 1977, *Astr. Ap.*, **54**, 593.
Booth, R. S., Kus, A. J., Norris, R. P., and Porter, N. D. 1981, *Nature*, **290**, 382.
Bowers, P. F. 1975, *A.J.*, **80**, 512.
———. 1981, *A.J.*, **86**, 1930.
———. 1985, in *Mass Loss from Red Giants*, ed. M. Morris and B. Zuckerman (*Ap. Space Sci. Lib.*, **117**, 189).
Bowers, P. F., and Johnston, K. J. 1988, *Ap. J.*, **330**, 339.
Bowers, P. F., Johnston, K. J., and Spencer, J. H. 1983, *Ap. J.*, **274**, 733.
Bujarrabal, V., Planesas, P., Gómez-González, J., Martin-Pintado, J., and del Romero, A. 1986, *Astr. Ap.*, **162**, 157.
Chapman, J. M. 1988, *M.N.R.A.S.*, **230**, 415.
Chapman, J. M., and Cohen, R. J. 1986, *M.N.R.A.S.*, **220**, 513.
Chapman, J. M., Cohen, R. J., Norris, R. P., Diamond, P. J., and Booth, R. 1984, *M.N.R.A.S.*, **207**, 149.
Claussen, M. J., and Fix, J. D. 1982, *Ap. J.*, **263**, 153.
Cohen, R. J., Downs, G., Emerson, R., Grimm, M., Gulkis, S., Stevens, G., and Tarter, J. 1987, *M.N.R.A.S.*, **225**, 491.
Cooke, B., and Elitzur, M. 1985, *Ap. J.*, **295**, 175.
Corbin, T. 1979, in *IAU Colloquium 48, Modern Astrometry*, ed. F. V. Prochazka and R. H. Tucker (Vienna: Vienna University Observatory), p. 505.
Deguchi, S. 1982, *Ap. J.*, **259**, 634.
de Vegt, C., Kleine, T., Johnston, K. J., Bowers, P. F., and Spencer, J. H. 1987, *Astr. Ap.*, **179**, 322.
Diamond, P. J., Johnston, K. J., Chapman, J. M., Lane, A. P., Bowers, P. F., Spencer, J. H., and Booth, R. S. 1987, *Astr. Ap.*, **174**, 95.
Diamond, P. J., Norris, R. P., and Booth, R. S. 1983, *Astr. Ap.*, **124**, L4.
Diamond, P. J., Norris, R. P., Rowland, P. R., Booth, R. S., and Nyman, L.-Å. 1985, *M.N.R.A.S.*, **212**, 1.
Dickinson, D. F., Kollberg, E., and Yngvesson, S. 1975, *Ap. J.*, **199**, 131.
Dickinson, D. F., Reid, M. J., Morris, M., and Redman, R. 1978, *Ap. J.* (*Letters*), **220**, L113.
Dyck, H. M. 1987, in *Late Stages of Stellar Evolution*, ed. S. Kwok and S. R. Pottasch (*Ap. Space Sci. Lib.*, **132**, 19).
Dyck, H. M., Zuckerman, B., Leinert, C., and Beckwith, S. 1984, *Ap. J.*, **287**, 801.
Elitzur, M., Goldreich, P., and Scoville, N. 1976, *Ap. J.*, **205**, 384.
Engels, D., Schmid-Burgk, J., and Walmsley, C. M. 1988, *Astr. Ap.*, **191**, 283.
Fillit, R., Proust, D., and Lépine, J. R. D. 1977, *Astr. Ap.*, **58**, 281.
Fix, J. D., 1987, *A.J.*, **93**, 433.
Goldreich, P., and Scoville, N. 1976, *Ap. J.*, **205**, 144.
Hartmann, L., and MacGregor, K. B. 1980, *Ap. J.*, **242**, 260.
Herman, J., Baud, B., Habing, H. J., and Winnberg, A. 1985, *Astr. Ap.*, **143**, 122.
Herman, J., and Habing, H. J. 1985, *Astr. Ap. Suppl.*, **59**, 523.
Högbom, J. A. 1974, *Astr. Ap. Suppl.*, **15**, 417.
Holzer, T. E., Flå, T., and Leer, E. 1983, *Ap. J.*, **275**, 808.
Holzer, T. E., and MacGregor, K. B. 1985, in *Mass Loss from Red Giants*, ed. M. Morris and B. Zuckerman (*Ap. Space Sci. Lib.*, **117**, 229).
Huggins, P. J., and Glassgold, A. E. 1982, *A.J.*, **87**, 1828.
Humphreys, R. M. 1975, *Pub. A.S.P.*, **87**, 433.
Jewell, P. R., Dickinson, D. F., Snyder, L. E., and Clemens, D. P. 1987, *Ap. J.*, **323**, 749.
Johansson, L. E. B., Andersson, C., Goss, W. M., and Winnberg, A. 1977, *Astr. Ap.*, **54**, 323.
Johnston, K. J., de Vegt, C., Florkowski, D. R., and Wade, C. M. 1985*a*, *A.J.*, **90**, 2390.
Johnston, K. J., Migenes, V., and Norris, R. 1989, *Ap. J.*, in press.
Johnston, K. J., Spencer, J. H., and Bowers, P. F. 1985, *Ap. J.*, **290**, 660.
Johnston, K. J., Wade, C. M., Florkowski, D. R., and de Vegt, C. 1985*b*, *A.J.*, **90**, 1343.
Jura, M. 1983, *Ap. J.*, **275**, 683.
Kahn, F. D., and West, K. A. 1985, *M.N.R.A.S.*, **212**, 837.
Kaifu, N., Buhl, D., and Snyder, L. E. 1975, *Ap. J.*, **195**, 359.
Knapp, G. R. 1985, *Ap. J.*, **293**, 273.
Knapp, G. R., and Morris, M. 1985, *Ap. J.*, **292**, 640.
Kwok, S. 1976, *J.R.A.S. Canada*, **70**, 49.
———. 1987, *Phys. Rept.*, **156**, 111.
Kwok, S., Purton, C. R., and Fitzgerald, M. P. 1978, *Ap. J.* (*Letters*), **219**, L125.
Lada, C. J., Blitz, L., Reid, M. J., and Moran, J. M. 1981, *Ap. J.*, **243**, 769.
Lane, A. P. 1982, Ph.D. thesis, University of Massachusetts.
Lane, A. P., Johnston, K. J., Bowers, P. F., Spencer, J. H., and Diamond, P. J. 1987, *Ap. J.*, **323**, 756.
Mamon, G. A., Glassgold, A. E., and Huggins, P. J. 1988, *Ap. J.*, **328**, 797.
Morris, M. 1987, *Pub. A.S.P.*, **99**, 1115.
Morris, M., Bowers, P. F., and Turner, B. E. 1982, *Ap. J.*, **259**, 625.
Morris, M., Redman, R., Reid, M. J., and Dickinson, D. F. 1979, *Ap. J.*, **229**, 257.
Netzer, N., and Knapp, G. R. 1987, *Ap. J.*, **323**, 734.
Nguyen-Q-Rieu, Deguchi, S., Izumiura, H., Kaifu, N., Ohishi, M., Suzuki, H., and Ukita, N. 1988, *Ap. J.*, **330**, 374.
Nguyen-Q-Rieu, Laury-Micolaut, C., Winnberg, A., and Schultz, G. V. 1979, *Astr. Ap.*, **75**, 351.
Nyman, L.-Å., and Olofsson, H. 1985, *Astr. Ap.*, **147**, 309.
———. 1986, *Astr. Ap.*, **158**, 67.
Reid, M. J., Moran, J. M., Leach, R. W., Ball, J. A., Johnston, K. J., Spencer, J. H., and Swenson, G. W. 1979, *Ap. J.* (*Letters*), **227**, L89.
Reid, M. J., Muhleman, D. O., Moran, J. M., Johnston, K. J., and Schwartz, P. R. 1977, *Ap. J.*, **214**, 60.
Rowan-Robinson, M., and Harris, S. 1983, *M.N.R.A.S.*, **202**, 767.
Schwan, H. 1988, private communication.
Silverglate, P., Zuckerman, B., Terzian, Y., and Wolff, M. 1979, *A.J.*, **84**, 345.
Sivagnanam, P., Diamond, P. J., LeSqueren, A. M., Daigne, G., Biraud, F., Ortega-Molina, A., and Graham, D. A. 1988, *Astr. Ap.*, **194**, 157.
Snyder, L. E., and Buhl, D. 1975, *Ap. J.*, **197**, 329.
Spencer, J. H., Winnberg, A., Olnon, F. M., Schwartz, P. R., Matthews, H. E., and Downes, D. 1981, *A.J.*, **86**, 392.
Sun, J., and Kwok, S. 1987, *Astr. Ap.*, **185**, 258.
Ukita, N., and LeSqueren, A. M. 1984, *Astr. Ap.*, **138**, 343.
Van Blerkom, D. 1978, *Ap. J.*, **233**, 835.
Van Blerkom, D., and Auer, L. 1976, *Ap. J.*, **204**, 775.
Wannier, P. G., and Sahai, R. 1986, *Ap. J.*, **311**, 335.
Welty, A. D., Fix, J. D., and Mutel, R. L. 1987, *Ap. J.*, **318**, 852.
Willson, L. A. 1987, in *Late Stages of Stellar Evolution*, ed. S. Kwok and S. R. Pottasch (*Ap. Space Sci. Lib.*, **132**, 253).
Wilson, W. J., Barrett, A. H., and Moran, J. M. 1970, *Ap. J.*, **160**, 545.
Witzel, A., and Johnston, K. J. 1982, *Abh. Hamburger Sternw.*, **10**, 3.
Zhou Zhen-pu, and Kaifu, N. 1984, *Astr. Ap.*, **138**, 359.
Zuckerman, B., and Aller, L. 1986, *Ap. J.*, **301**, 772.
Zuckerman, B., and Dyck, H. M. 1986, *Ap. J.*, **304**, 394.
Zuckerman, B., and Gatley, I. 1988, *Ap. J.*, **324**, 501.

P. F. BOWERS and K. J. JOHNSTON: Code 4130, Naval Research Laboratory, Washington, DC 20375-5000

C. DE VEGT: Hamburger Sternwarte, Universität Hamburg, Gojenbergsweg 112, D-2050 Hamburg 80, Federal Republic of Germany